NASA
Technical
Paper
3099

1991

Effects of Yaw Angle and Reynolds Number on Rectangular-Box Cavities at Subsonic and Transonic Speeds

E. B. Plentovich,
Julio Chu,
and M. B. Tracy
Langley Research Center
Hampton, Virginia

National Aeronautics and
Space Administration
Office of Management
Scientific and Technical
Information Program

Summary

An experimental investigation was conducted to determine the effect of Reynolds number (separate from boundary-layer thickness) and the effect of yaw angle on the pressure distribution in a rectangular-box cavity. The cavity was tested at Mach numbers from 0.20 to 0.90, Reynolds numbers from 2×10^6 to 100×10^6 ft^{-1}, and yaw angles of 0° and 15°. Cavities were tested with length-to-depth ratios l/h of 4.4, 6.7, 12.67, and 20.0. Fluctuating- and static-pressure data on the model walls were obtained and a complete tabulation of the mean static-pressure data is presented. (The static-pressure data are analyzed in this report.) The cavity model was mounted in the sidewall of the Langley 0.3-Meter Transonic Cryogenic Tunnel. The thickness of the sidewall boundary layer entering the cavity was measured with a pitot pressure rake and the tabulated values are provided. Over the range of Reynolds numbers tested, the ratio of boundary-layer thickness to cavity depth was approximately constant. There was no significant effect of Reynolds number on the static-pressure distributions. The effect of yaw on the cavity pressure distribution was most pronounced when the flow field was of the open type at 0° yaw. In such cases the flow field became transitional when the cavity was positioned at 15° yaw. However, if the flow field at 0° yaw was transitional or closed, the effect of 15° yaw on the pressure distribution was very minimal. This test also showed that the types of flow field observed for given ranges of l/h at supersonic conditions would occur for different ranges of l/h at subsonic and transonic conditions.

Introduction

The flow field within a rectangular-box cavity has been studied for many years both experimentally and computationally (refs. 1 to 13). Much of the research has been directed at developing an understanding of the flow fields that exist within cavities for the purpose of creating an environment from which stores, internal to an aircraft, can be released. Most of the studies have been conducted at relatively low Reynolds numbers based on cavity length ($R_l \leq 15 \times 10^6$) and with the cavity aligned with the free-stream flow direction (0° yaw). Therefore, an investigation was conducted to determine the effect of Reynolds number at a nearly constant boundary-layer thickness and the effect of yaw on cavity flow fields at subsonic and transonic speeds. A rectangular-box cavity model was mounted in the sidewall of the Langley 0.3-Meter Transonic Cryogenic Tunnel (TCT). Fluctuating- and static-pressure data on the model were obtained at Mach numbers from 0.20 to 0.90, Reynolds numbers from 2×10^6 to 100×10^6 ft^{-1} (R_l from 1.9×10^6 to 94.0×10^6), and yaw angles of 0° and 15°. The static-pressure data are analyzed in this report and the fluctuating-pressure data are discussed in reference 14.

Symbols

C_p	pressure coefficient, $\frac{p - p_\infty}{q_\infty}$
h	cavity depth, in.
l	cavity length, in.
M_∞	free-stream Mach number
n	index in power law for velocity profile ($u \propto z^{1/n}$)
p	measured surface static pressure, psf
p_∞	free-stream static pressure, psf
$p_{t,\infty}$	free-stream total pressure, psf
q_∞	free-stream dynamic pressure, psf
R	free-stream unit Reynolds number, ft^{-1}
R_l	Reynolds number based on cavity length
$T_{t,\infty}$	free-stream total temperature, K
u	velocity, ft/sec
u_{bl}/u_∞	ratio of local velocity in boundary layer to free-stream velocity
w	cavity width, in.
x	distance in streamwise direction (see fig. 6), in.
y	distance in spanwise direction (see fig. 6), in.
z	distance normal to tunnel sidewall, in.
δ	boundary-layer thickness, in.
δ^*	boundary-layer displacement thickness, in.
θ	boundary-layer momentum thickness, in.
ψ	yaw angle, deg

Experimental Methods

Wind Tunnel Description

The tests were conducted in the two-dimensional adaptive wall test section of the Langley 0.3-Meter Transonic Cryogenic Tunnel (TCT). A sketch of the tunnel is presented in figure 1. The 0.3-m TCT is a fan-driven, cryogenic pressure tunnel that uses gaseous nitrogen as a test medium. It is capable of operating at stagnation temperatures from approximately 80 K to 327 K and at stagnation pressures from 1.2 atm to 6.0 atm. The fan speed is variable so that the Mach number of the empty test section can be varied continuously from about 0.20 to 0.95. This combination of test conditions provides a test envelope of Reynolds numbers up to about 100×10^6 based on a model length of 1 ft. Additional details of the tunnel and its range of operation may be found in references 15 and 16.

A sketch showing details of the flow region in the adaptive wall test section is presented in figure 2, and figure 3 is a photograph of the test section. The test section is 13 in. by 13 in. in cross section at the entrance. All four walls are solid. The sidewalls are rigid, whereas the top and bottom walls are flexible and moveable. The flexible top and bottom walls are computer controlled, with feedback provided on the wall position and the top and bottom wall pressure distribution. The basic objective is to align the test section boundaries with the model streamlines such that the flow field in the vicinity of the model approaches that which would be obtained for free-air conditions. When the walls are positioned in this way they are said to be *streamlined*. Specific information on the adaptive wall test section and a brief description of the strategy used to contour the walls can be found in reference 17. Specific details on the contouring strategy for the flexible walls are given in reference 18.

The 0.3-m TCT model mounting system is designed for two-dimensional models. Typically, the model is supported between two turntables centered 30.7 in. downstream of the test section entrance. Models with lengths up to 13 in. can be tested over an angle-of-attack range of 40°. The turntables are driven by an electric stepper motor that is connected through a yoke to the perimeter of both turntables. This arrangement drives both turntables to eliminate possible model twisting. The angular position of the turntables and, therefore, the geometric angle of attack of the model are measured with a digital shaft encoder geared to one turntable.

The 0.3-m TCT has a sidewall boundary-layer-removal system to reduce the boundary-layer thickness (ref. 19). This system uses porous plates just upstream of the model mounting turntables. The boundary-layer thickness is not reduced much with the use of the boundary-layer-removal system (ref. 19), so it was decided not to use the system and to replace the porous plates used for boundary-layer removal with solid plates. The location of the boundary-layer-removal plates relative to the model position is shown in figure 2.

Model Description

The model tested was a rectangular-box cavity mounted on the sidewall of the tunnel. The cavity model was centered on the turntable at about station 0. (See fig. 2.) The position of the turntable in the test section is shown in figure 2. The model was fabricated to allow the use of the angle-of-attack drive for positioning the cavity at yaw angles of 0° and 15°. Because of the cavity model geometry, the encoder that is generally used to measure the turntable position could not be utilized for this test. Therefore, an accelerometer that was calibrated for 0° and 15° of yaw was used to determine the turntable and cavity model position. The accelerometer responds to being tilted in the Earth's gravitational field and the output of the accelerometer is a function of the sine of the angle of inclination. The accelerometer is capable of resolving angles to within ±0.015° at 15°.

The cavity had a length l of 11.25 in., a width w of 2.50 in., and a maximum depth h of 2.56 in. The floor of the cavity could be positioned at various depths to vary l/h with the length and width fixed. The l/h values tested were 4.4 (h = 2.56 in.), 6.7 (h = 1.68 in.), 12.67 (h = 0.89 in.), and 20.0 (h = 0.56 in.). A configuration with the floor mounted flush with the tunnel sidewall, having no cavity, was used when the boundary-layer thickness approaching the cavity was determined. Photographs of the model are provided in figures 4 and 5. Figure 4 shows the model prior to tunnel installation, with the floor of the cavity positioned at a depth of 2.56 in. (l/h = 4.4). Figure 5 shows the model mounted in the tunnel in the configuration for measuring the boundary layer (no cavity and the boundary-layer rake installed).

The model was instrumented with 21 static-pressure orifices and 18 flush-mounted fluctuating-pressure transducers, as shown in figure 6. The forward and aft walls of the cavity were instrumented with only a single fluctuating-pressure transducer located at half the depth of the cavity. Table I provides the measured positions of the static-pressure ports.

Test Conditions

The model was tested at Mach numbers from 0.20 to 0.90, Reynolds numbers from 2×10^6 to 100×10^6 ft^{-1}, and $\psi = 0°$ and 15°. The boundary-layer thickness was nearly constant throughout the range of Reynolds numbers tested. The model was tested at a reduced set of conditions and configurations for $\psi = 15°$. Table II provides a summary of the nominal test conditions and model configurations. The flexible test section walls were set to a streamlined shape for each test condition. This resulted in wall deflections for each condition that were no greater than ±0.04 in. for each wall.

Measurements

Surface static pressures. Because of the large changes in dynamic pressure in the 0.3-m TCT over its operational range (a factor of about 75), a high-precision capacitive-type transducer is used for pressure measurements. The electrical outputs from the transducers are connected to individual signal conditioners. The signal conditioners are autoranging to keep the electrical output to the data acquisition system at a high level for all pressure ranges. The transducers have a maximum range from −100 psi to 100 psi and have an accuracy of ±0.25 percent of reading from 25 percent of negative full scale to 100 percent of positive full scale. Additional details of the 0.3-m TCT pressure instrumentation system can be found in reference 15.

For the experimental data reported herein, each orifice was sampled 40 times over a 1-sec period. These data were then averaged to produce the mean value for each data point.

Boundary-layer thickness. The ratio of boundary-layer thickness to cavity depth has been shown to be an important similarity parameter in the study of cavity flows (ref. 3). To determine the boundary-layer thickness at the cavity leading edge (the tunnel sidewall boundary-layer thickness), the cavity floor was moved flush with the sidewall (i.e., no cavity existed) and the pitot pressure through the boundary layer was measured with a rake at the cavity leading edge. A drawing of the rake is shown in figure 7. The boundary-layer rake pressures were measured with high-precision capacitive-type transducers similar to those used for the surface static-pressure measurements. The reference pressure for these transducers was the tunnel plenum static pressure. The boundary layer entering the cavity (the tunnel sidewall boundary layer) has been shown to be turbulent (ref. 20).

For calculations of Mach number through the boundary layer, the static pressure at the position of the rake was needed. (Static pressure through the boundary layer is assumed to be constant.) The measurements from the static-pressure ports near the boundary-layer rake were influenced by the rake and were therefore in error, so the local wall static pressure was assumed to be equal to the tunnel static pressure.

To estimate the boundary-layer thickness δ from the rake pitot pressure measurements, the data were reduced using the method described in reference 21. This method assumes a power-law variation for the turbulent-boundary-layer velocity profile. A least-squares fit to the calculated values of u_{bl}/u_∞ is made to determine the values of δ and n, the power-law index. Values for displacement thickness δ^* and momentum thickness θ are calculated using numerical integration. For the boundary-layer parameters calculated herein, only the pressure data from boundary-layer rake tubes within the boundary layer ($u_{bl}/u_\infty \leq 0.99$) were used for the calculations. Because of the nature of the least-squares fit, additional points outside the boundary layer (within the free stream) would introduce increasing error into the estimations. The calculated boundary-layer parameters are presented in table III and a plot of the boundary-layer thickness over the range of Reynolds numbers tested is shown in figure 8. The pitot pressures through the boundary layer were not measured at all nominal test conditions, as shown in table II ($l/h = \infty$), because of tunnel time constraints.

Tabulated data. The cavity pressure measurements were reduced to coefficient form and are presented in tables IV to X. These tables contain the tunnel test conditions as well as the mean values of the measured pressures. The pressure data are presented as CPxx, where the xx refers to the orifice number. (The locations of the orifices are presented in table I.) Data are presented in order of increasing Mach number and Reynolds number for each configuration.

Discussion of Results

At supersonic speeds, four types of mean cavity flow have been defined (refs. 4 and 13) and are sketched in figure 9. The first type occurs when the cavity is "deep" ($l/h < 10$) and is termed *open cavity flow.* For open cavity flow, the flow essentially bridges the cavity and a shear layer is formed over the cavity. A weak shock can form near the leading edge of the cavity as a result of the flow being compressed slightly by the shear layer. The second type of cavity flow is for "shallow" cavities ($l/h > 13$) and is termed *closed cavity flow.* In closed cavity flow, the flow separates at the forward face of the cavity, reattaches at some point along the cavity floor, and separates again before reaching the rear cavity face. This creates two distinct separation regions, one downstream of the forward face and one upstream of the rear face. The third and fourth mean flow types (*transitional-closed cavity flow* and *transitional-open cavity flow*) have in the past both been referred to as transitional flow, that is, where the flow field changes from closed to open cavity flow. This change generally occurs for l/h between 10 and 13. The determination of transitional-closed and transitional-open flows, as well as determination of open and closed flows, can best be made by observation of the pressure distribution in the cavity. Figure 9 provides a guideline for determining the type of cavity flow, though it must be recognized that the transonic characteristics may not be identical to supersonic characteristics.

Although at supersonic speeds acoustic pressure fluctuations have been observed in cavities with open cavity flow, there do not appear to be large variations in the static-pressure measurements. At lower speeds, large variations in instantaneous pressure measurements have been observed (refs. 5 and 22). It is possible to obtain repeatable mean values if a sufficiently high sample rate is used, but a large variation in amplitude and shape of instantaneous pressure distributions in deep cavities at transonic and subsonic speeds remains.

Effect of Test Conditions

The data in figure 10 show the effect of tunnel conditions on the repeatability of pressure distributions on the cavity floor. The 0.3-m TCT can operate over a large temperature and pressure range, with constant Mach and Reynolds numbers able to be obtained at many combinations of temperature and pressure. To address concerns about the effect of temperature on the dynamic-pressure transducers, additional points were included in the test matrix to repeat a given Mach number and Reynolds number at different temperatures and pressures. (See table II.) An attempt was also made to obtain as wide a range of Reynolds numbers as possible at the same temperature to allow for data comparison in case the temperature did affect the measurements. The effect of temperature and pressure on M_∞ and R for the $l/h = 4.4$ cavity configuration is shown in figure 10. Figure 10(a) is a comparison of data taken at $M = 0.60$ and $R = 30 \times 10^6$ at the same temperature and pressure (a repeat point), and figure 10(b) shows a comparison of data taken at $M = 0.60$ and $R = 30 \times 10^6$ at different temperatures and pressures. For both cases the static-pressure data repeat well and the tunnel conditions do not significantly affect the data.

Effect of Reynolds Number

The effect of Reynolds number on cavity flow fields was a principal focus of this test. In most tests, a change in Reynolds number is usually associated with a change in δ. In this study, however, the boundary layer approaching the cavity was the tunnel sidewall boundary layer, which is relatively thick and insensitive to changes in Reynolds number. (Fig. 8 provides a plot showing the change in δ with Reynolds number.) The value of δ/h changed little compared with the change in free-stream Reynolds number (at least a factor of 10), and thus the effects shown are attributed essentially to changes in Reynolds number.

Figures 11 to 14 show the effect of Reynolds number at constant Mach numbers for the various cavity configurations at $\psi = 0°$. As shown in the plots, there is very little change in the mean C_p distribution over the range of Reynolds numbers tested.

The pressure distributions at $\psi = 15°$ are provided in figures 15 to 17. For the majority of the data there are only slight differences in the measured pressures, and these differences would indicate minimal effect on flow-field characteristics. The largest influence of Reynolds number on the pressure distribution is shown in figure 15(a). However, for these data it appears that the flow field maintains a transitional-closed characteristic. (Data were not taken for the $l/h = 20.0$ cavity configuration at $\psi = 15°$.)

Effect of l/h Change

Figures 18 and 19 provide a comparison of cavity pressure measurements for the different cavity configurations. The cavity length remained fixed at 11.25 in., but depth was varied to generate cavities with l/h of 4.4, 6.7, 12.67, and 20.0. Because of the minimal variation in pressure distribution with Reynolds number this comparison is only shown for $R \approx 90 \times 10^6$. Figure 18 shows the data for $\psi = 0°$, and as previously discussed, the cavity with $l/h = 4.4$ has open flow and $l/h = 20.0$ has closed flow. The cavity with $l/h = 6.7$ was expected to have an open flow field, but the pressure distribution shows that it is a transitional-open flow field at $M_\infty = 0.60$ and tends more toward the open type at higher Mach numbers. Also, a cavity with $l/h = 12.67$ would be expected to be transitional in nature; however, at $M_\infty = 0.60$ the flow field is closed and becomes transitional-closed at higher Mach numbers.

Figure 19 shows the data for $\psi = 15°$ and $R \approx 90 \times 10^6$. Here the flow is transitional-closed for

$l/h = 4.4$ and 6.7; however, for $l/h = 12.67$ the flow is of the closed type.

Effect of Mach Number

The cavity pressure distributions for several Mach numbers at constant Reynolds numbers are presented in figures 20 to 23. Each figure shows data for a separate cavity l/h at $\psi = 0°$. The data at $M_\infty = 0.20$ have characteristics distinct from those of the flow fields at higher Mach numbers. These characteristics were also observed at $M_\infty = 0.30$ in reference 22 and indicate that the flow-field characteristics at low subsonic speeds are significantly different than the characteristics at higher speeds. As mentioned previously, in the supersonic speed regime the $l/h = 6.7$ cavity would be expected to be open and the $l/h = 12.67$ cavity would be transitional. However, figure 21 again shows that the $l/h = 6.7$ cavity is transitional-open at $M_\infty = 0.60$ and is changing toward an open type at higher Mach numbers. Figure 22 shows that the $l/h = 12.67$ configuration changes from a closed cavity flow field to a transitional-closed cavity flow field as Mach number is increased. In figure 23 the flow field remains closed at all Mach numbers tested.

Figures 24 to 26 show the effect of Mach number on the cavity flow field at $\psi = 15°$. The pressure distributions for $l/h = 4.4$ and 6.7 give the appearance of a transitional-closed cavity flow (figs. 24 and 25). In figure 26, pressure distributions for $l/h = 12.67$ show that the flow field is closed at $M_\infty = 0.60$ and 0.80 and closed on the verge of transitional-closed at $M_\infty = 0.90$.

Effect of Yaw Angle

Figures 27 to 29 present mean pressure distributions for the two yaw angles tested at various Mach numbers for $l/h = 4.4$, 6.7, and 12.67. (The $l/h = 20.0$ cavity configuration was not tested at $\psi = 15°$.) Recall that the pressures were measured along the centerline of the model, so at $\psi = 15°$ the pressures are skewed with respect to the free-stream flow. The effect of yaw angle on a closed or a transitional cavity flow field is minimal. (See figs. 28(c), 28(d), and 29.) However, if the flow field is open at $\psi = 0°$, when the cavity is yawed to 15° the flow field becomes transitional and a much larger change in the mean pressures is present (figs. 27, 28(a), and 28(b)).

Concluding Remarks

To provide information on the effect of Reynolds numbers (independent of boundary-layer thickness) on cavity flow fields at subsonic and transonic speeds, an experimental study was conducted in the Langley 0.3-Meter Transonic Cryogenic Tunnel. For this study, cavities with length-to-height ratios l/h of 4.4, 6.7, 12.67, and 20.0 were tested at Mach numbers from 0.20 to 0.90 and at Reynolds numbers from 2×10^6 to 100×10^6 ft^{-1}. Static and fluctuating pressures were measured on the model and the boundary-layer thickness was measured at the cavity leading edge. The Reynolds numbers tested (the ratio of boundary-layer thickness to cavity depth was approximately constant) had no significant effect on the static-pressure distribution. The effect of yaw on the cavity mean pressure distribution was most pronounced if the flow field was of the open type at 0° yaw. In such cases the flow field became transitional when the cavity was positioned at 15° yaw. However, if the flow field at 0° yaw was transitional or closed, the effect of yaw on the cavity pressure distribution was very minimal. This test also showed that the types of flow field observed for given ranges of l/h at supersonic conditions would occur for different ranges of l/h at subsonic and transonic conditions.

NASA Langley Research Center
Hampton, VA 23665-5225
April 15, 1991

References

1. Rossiter, J. E.: *Wind-Tunnel Experiment on the Flow Over Rectangular Cavities at Subsonic and Transonic Speeds.* R. & M. No. 3438, British Aeronautical Research Council, Oct. 1964.
2. Kaufman, Louis G., II; Maciulaitis, Algirdas; and Clark, Rodney L.: *Mach 0.6 to 3.0 Flows Over Rectangular Cavities.* AFWAL-TR-82-3112, U.S. Air Force, May 1983. (Available from DTIC as AD A134 579.)
3. Charwat, A. F.; Roos, J. N.; Dewey, F. C., Jr.; and Hitz, J. A.: An Investigation of Separated Flows—Part I: The Pressure Field. *J. Aeronaut. Sci.*, vol. 28, no. 6, June 1961, pp. 457–470.
4. Stallings, Robert L., Jr.; and Wilcox, Floyd J., Jr.: *Experimental Cavity Pressure Distributions at Supersonic Speeds.* NASA TP-2683, 1987.
5. Dix, Richard E.: On Simulation Techniques for the Separation of Stores From Internal Installations. SAE Tech. Paper Ser. 871799, Oct. 1987.
6. Heller, Hanno H.; and Bliss, Donald B.: *Aerodynamically Induced Pressure Oscillations in Cavities—Physical Mechanisms and Suppression Concepts.* Tech. Rep. AFFDL-TR-74-133, U.S. Air Force, Feb. 1975.

7. Baysal, O.; Srinivasan, S.; and Stallings, L., Jr.: Unsteady Viscous Calculations of Supersonic Flows Past Deep and Shallow Three-Dimensional Cavities. AIAA-88-0101, Jan. 1988.

8. Catalano, George D.: *Turbulent Flow Over an Embedded Rectangular Cavity.* AFATL-TR-86-73, U.S. Air Force, Feb. 1987. (Available from DTIC as AD A177 928.)

9. Om, Deepak: Navier-Stokes Simulation for Flow Past an Open Cavity. AIAA-86-2628, Oct. 1986.

10. Baysal, O.; and Stallings, R. L., Jr.: Computational and Experimental Investigation of Cavity Flowfields. AIAA-87-0114, Jan. 1987.

11. Suhs, N. E.: Computations of Three-Dimensional Cavity Flow at Subsonic and Supersonic Mach Numbers. AIAA-87-1208, June 1987.

12. Srinivasan, S.; Baysal, O.; and Plentovich, E. B.: Navier-Stokes Calculations of Transonic Flows Past Open and Transitional Cavities. *Advances and Applications in Computational Fluid Dynamics*, O. Baysal, ed., FED-Vol. 66, American Soc. of Mechanical Engineers, 1988, pp. 169–179.

13. Wilcox, Floyd J., Jr.: Experimental Measurements of Internal Store Separation Characteristics at Supersonic Speeds. *Store Carriage, Integration and Release*, Royal Aeronautical Soc., 1990, pp. 5.1–5.16.

14. Tracy, M. B.; Plentovich, E. B.; Chu, J.; and Shearin, J. G.: Cavity Acoustics in High Reynolds Number Transonic Flows. *Proceedings 8th JOCG Aircraft/Stores Compatibility Symposium*, Joint Ordnance Commanders Group, Aircraft/Stores Compatibility Subgroup, and American Inst. of Aeronautics and Astronautics, Oct. 1990, pp. 25-1–25-28.

15. Ladson, Charles L.; and Ray, Edward J.: *Evolution, Calibration, and Operational Characteristics of the Two-Dimensional Test Section of the Langley 0.3-Meter Transonic Cryogenic Tunnel.* NASA TP-2749, 1987.

16. Rallo, Rosemary A.; Dress, David A.; and Siegle, Henry J. A.: *Operating Envelope Charts for the Langley 0.3-Meter Transonic Cryogenic Wind Tunnel.* NASA TM-89008, 1986.

17. Mineck, Raymond E.: *Hardware and Operating Features of the Adaptive Wall Test Section for the Langley 0.3-Meter Transonic Cryogenic Tunnel.* NASA TM-4114, 1989.

18. Wolf, Stephen W. D.; and Goodyer, Michael J.: *Predictive Wall Adjustment Strategy for Two-Dimensional Flexible Walled Adaptive Wind Tunnel—A Detailed Description of the First One-Step Method.* NASA CR-181635, 1988.

19. Murthy, A. V.: *Sidewall Boundary-Layer Measurements With Upstream Suction in the Langley 0.3-Meter Transonic Cryogenic Tunnel.* NASA CR-4192, 1988.

20. Murthy, A. V.; Johnson, Charles B.; Ray, Edward J.; Lawing, Pierce L.; and Thibodeaux, Jerry J.: *Studies of Sidewall Boundary Layer in the Langley 0.3-Meter Transonic Cryogenic Tunnel With and Without Suction.* NASA TP-2096, 1983.

21. Murthy, A. V.: *Calculation of Sidewall Boundary-Layer Parameters From Rake Measurements for the Langley 0.3-Meter Transonic Cryogenic Tunnel.* NASA CR-178241, 1987.

22. Plentovich, E. B.: *Three-Dimensional Cavity Flow Fields at Subsonic and Transonic Speeds.* NASA TM-4209, 1990.

Table I. Locations of Static-Pressure Orifices

Orifice no.	x, in.	y, in.	z, in.	Model location
1	0.350	0	$-h$	Cavity floor
2	2.050			
3	2.854			
4	3.658			
5	4.462			
6	5.266			
7	6.071			
8	6.874			
9	7.678			
10	8.482			
11	9.286			
12	10.090			
13	10.894			
14	.800	.5		
15	.800	−.5		
16	5.666	.5		
17	10.486	.5		
18	10.486	−.5		
19	−.690	.5	0	Tunnel sidewall, forward of cavity
20	−.230	.5	0	Tunnel sidewall, forward of cavity
21	11.800	.5	0	Tunnel sidewall, aft of cavity

Table II. Nominal Test Matrix

M_∞	R, ft^{-1}	$p_{t,\infty}$, psi	$T_{t,\infty}$, K	$\psi = 0^\circ$ and l/h of—					$\psi = 15^\circ$ and l/h of—		
				4.4	6.7	12.67	20.0	∞[1]	4.4	6.7	12.67
0.20	2×10^6	22.5	310	×	×				×	×	
.20	10	26.0	105	×	×				×	×	
.20	30	76.0	105	×	×				×	×	
.60	4	19.0	320	×	×	×	×	×	×	×	×
.60	10	46.0	320	×	×	×	×	×			
.60	10	21.0	180	×	×	×	×	×	×	×	×
.60	30	64.0	180	×	×	×	×	×			
.60	30	30.0	105	×	×	×	×	×	×	×	×
.60	80	77.0	105	×	×	×	×	×	×	×	×
.60	90	86.0	105	×	×	×	×	×	×	×	×
.80	5	18.0	310	×	×	×	×	×	×	×	×
.80	10	37.0	310	×	×	×	×	×	×		
.80	10	21.0	200	×	×	×	×	×	×	×	×
.80	30	62.0	200	×	×	×	×	×			
.80	30	26.0	105	×	×	×	×	×	×	×	×
.80	80	64.0	105	×	×	×	×	×	×	×	×
.80	90	72.0	105	×	×	×	×	×	×	×	×
.80	100	85.0	105	×	×	×	×	×	×	×	×
.90	10	19.5	200	×	×	×	×	×	×	×	×
.90	30	68.0	200	×	×	×	×	×			
.90	30	22.5	105	×	×	×	×	×	×	×	×
.90	80	60.0	105	×	×	×	×	×	×	×	×
.90	90	67.0	105	×	×	×	×	×	×	×	×
.90	100	75.0	105	×	×	×	×	×		×	×

[1]Cavity ceiling flush with sidewall for boundary-layer measurements.

Table III. Boundary-Layer Parameters

M_∞	R, ft^{-1}	$p_{t,\infty}$, psi	$T_{t,\infty}$, K	δ, in.	δ^*, in.	θ, in.
0.60	5×10^6	20	300	0.578	0.074	0.052
0.60	10	42	299	.518	.067	.047
0.60	10	21	180	.512	.067	.047
0.60	30	63	180	.475	.058	.042
0.60	30	33	115	.512	.063	.045
0.60	80	86	113	.464	.055	.049
0.60	85	88	110	.469	.057	.041
0.80	6	21	300	.513	.073	.047
0.80	10	35	300	.544	.071	.047
0.80	10	23	210	.505	.070	.046
0.80	30	66	209	.489	.064	.043
0.80	30	27	112	.494	.066	.043
0.80	80	71	112	.475	.059	.039
0.80	90	80	112	.463	.060	.039
0.80	100	87	111	.437	.059	.038
0.90	13	27	210	.511	.073	.046
0.90	30	26	114	.491	.064	.041
0.90	80	69	114	.463	.062	.039
0.90	90	77	114	.456	.060	.038
0.90	100	86	114	.458	.061	.039

Table IV. Pressure Coefficients for $l/h = 4.4$ Cavity at $\psi = 0°$

Run	Point	M_∞	$R \times 10^{-6}$	p_∞	$p_{t,\infty}$	q_∞	$T_{t,\infty}$	CP01	CP02	CP03	CP04	CP05	CP06	CP07	CP08	CP09	CP10	CP11
3.	11.	0.20	1.8	19.36	19.91	0.54	302.1	0.0235	0.0279	0.0044	−0.0003	−0.0148	−0.0246	−0.0425	−0.0851	−0.1364	−0.1464	−0.1087
10.	49.	0.20	10.1	24.71	25.42	0.70	104.2	0.0304	0.0408	0.0227	0.0181	−0.0009	−0.0199	−0.0458	−0.0861	−0.1348	−0.1587	−0.1116
10.	48.	0.20	29.8	73.06	75.14	2.06	104.1	0.0416	0.0572	0.0368	0.0251	−0.0038	−0.0273	−0.0785	−0.1199	−0.1679	−0.1728	−0.1178
3.	8.	0.60	4.0	13.17	16.83	3.34	299.4	−0.0141	−0.0242	−0.0251	−0.0279	−0.0325	−0.0349	−0.0370	−0.0385	−0.0367	−0.0236	0.0004
3.	15.	0.60	4.0	14.23	18.17	3.60	319.2	−0.0218	−0.0296	−0.0304	−0.0322	−0.0377	−0.0412	−0.0415	−0.0409	−0.0377	−0.0236	−0.0001
3.	16.	0.60	10.0	35.65	45.51	9.02	319.0	−0.0073	−0.0152	−0.0158	−0.0180	−0.0240	−0.0267	−0.0256	−0.0212	−0.0162	−0.0034	0.0226
13.	58.	0.60	10.1	16.51	21.14	4.23	179.9	−0.0181	−0.0282	−0.0277	−0.0305	−0.0366	−0.0408	−0.0442	−0.0462	−0.0424	−0.0284	−0.0006
13.	60.	0.60	30.1	49.74	63.45	12.54	179.6	−0.0166	−0.0250	−0.0254	−0.0289	−0.0370	−0.0416	−0.0427	−0.0361	−0.0306	−0.0141	0.0150
10.	45.	0.60	30.0	22.38	28.54	5.63	104.0	−0.0030	−0.0118	−0.0110	−0.0135	−0.0205	−0.0252	−0.0294	−0.0295	−0.0252	−0.0101	0.0191
14.	69.	0.60	30.1	22.74	29.02	5.74	104.9	0.0081	−0.0011	0.0003	−0.0036	−0.0093	−0.0139	−0.0170	−0.0176	−0.0154	−0.0036	0.0258
10.	46.	0.60	80.1	60.18	76.53	14.96	104.0	−0.0025	−0.0113	−0.0125	−0.0158	−0.0242	−0.0283	−0.0300	−0.0235	−0.0175	−0.0029	0.0274
10.	47.	0.60	90.0	67.62	85.98	16.79	104.0	−0.0059	−0.0148	−0.0142	−0.0179	−0.0258	−0.0330	−0.0331	−0.0258	−0.0203	−0.0070	0.0214
3.	9.	0.80	6.2	13.76	20.96	6.15	290.1	−0.0093	−0.0243	−0.0304	−0.0289	−0.0232	−0.0043	0.0095	0.0300	0.0609	0.1063	0.1487
3.	12.	0.80	10.1	23.19	35.26	10.33	298.6	−0.0082	−0.0241	−0.0306	−0.0307	−0.0221	−0.0026	0.0169	0.0383	0.0719	0.1170	0.1589
17.	101.	0.80	10.5	14.90	22.83	6.76	209.8	−0.0093	−0.0217	−0.0257	−0.0269	−0.0221	−0.0096	0.0052	0.0213	0.0516	0.0949	0.1389
17.	98.	0.80	10.1	14.97	22.83	6.72	214.8	−0.0177	−0.0307	−0.0352	−0.0358	−0.0309	−0.0192	−0.0053	0.0098	0.0400	0.0821	0.1262
17.	99.	0.80	30.1	43.09	65.55	19.22	209.2	−0.0264	−0.0380	−0.0422	−0.0445	−0.0441	−0.0366	−0.0238	−0.0036	0.0240	0.0633	0.1094
10.	44.	0.80	30.1	15.69	23.93	7.03	104.5	−0.0036	−0.0145	−0.0192	−0.0225	−0.0177	−0.0076	0.0065	0.0249	0.0548	0.0971	0.1435
14.	70.	0.81	30.1	15.77	24.13	7.14	105.1	−0.0085	−0.0186	−0.0236	−0.0268	−0.0244	−0.0163	−0.0044	0.0126	0.0384	0.0797	0.1240
14.	75.	0.80	79.9	48.24	73.34	21.45	114.9	−0.0254	−0.0336	−0.0373	−0.0419	−0.0437	−0.0383	−0.0271	−0.0098	0.0156	0.0555	0.0967
14.	76.	0.80	90.2	54.39	82.75	24.23	114.9	−0.0285	−0.0382	−0.0431	−0.0472	−0.0485	−0.0421	−0.0301	−0.0101	0.0167	0.0536	0.0976
14.	77.	0.81	99.5	56.98	87.29	25.81	112.0	−0.0307	−0.0415	−0.0465	−0.0504	−0.0521	−0.0479	−0.0367	−0.0163	0.0081	0.0428	0.0878
17.	97.	0.92	12.2	15.11	26.11	8.95	215.1	−0.0024	−0.0105	−0.0130	−0.0162	−0.0199	−0.0197	−0.0160	−0.0093	0.0077	0.0340	0.0691
17.	100.	0.89	30.0	36.75	61.76	20.57	209.3	−0.0284	−0.0362	−0.0372	−0.0409	−0.0463	−0.0472	−0.0439	−0.0344	−0.0182	0.0057	0.0449
14.	71.	0.90	30.0	15.23	25.73	8.62	114.3	−0.0182	−0.0250	−0.0263	−0.0294	−0.0308	−0.0285	−0.0225	−0.0132	0.0061	0.0364	0.0730
14.	74.	0.91	80.1	40.70	69.35	23.43	115.0	−0.0207	−0.0277	−0.0304	−0.0337	−0.0376	−0.0353	−0.0275	−0.0143	0.0053	0.0349	0.0725
14.	79.	0.91	90.0	43.76	74.82	25.36	112.0	−0.0029	−0.0091	−0.0121	−0.0159	−0.0179	−0.0158	−0.0082	0.0051	0.0250	0.0554	0.0944
14.	81.	0.92	99.1	49.71	85.79	29.36	115.1	−0.0124	−0.0190	−0.0205	−0.0240	−0.0268	−0.0267	−0.0189	−0.0080	0.0115	0.0406	0.0792

Table IV. Concluded

Run	Point	CP12	CP13	CP14	CP15	CP16	CP17	CP18	CP19	CP20	CP21
3.	11.	−0.0058	0.2122	0.0398	0.0128	−0.0041	0.1002	0.0846	0.0152	0.0151	0.0064
10.	49.	0.0121	0.2372	0.0318	0.0410	−0.0416	0.1024	0.1049	0.0244	0.0323	0.0221
10.	48.	0.0341	0.2694	0.0532	0.0522	−0.0566	0.1343	0.1266	0.0276	0.0401	0.0230
3.	8.	0.0369	0.1923	−0.0033	−0.0184	−0.0221	0.1084	0.0975	−0.0014	0.0005	−0.1266
3.	15.	0.0347	0.1874	−0.0216	−0.0269	−0.0398	0.0911	0.0924	−0.0081	−0.0069	−0.1416
3.	16.	0.0595	0.2100	−0.0123	−0.0133	−0.0320	0.1118	0.1173	0.0055	0.0117	−0.1203
13.	58.	0.0382	0.2024	−0.0185	−0.0220	−0.0384	0.1029	0.1019	−0.0075	−0.0010	−0.1120
13.	60.	0.0569	0.2103	−0.0173	−0.0181	−0.0352	0.1177	0.1161	−0.0039	0.0056	−0.1272
10.	45.	0.0608	0.2228	−0.0084	−0.0035	−0.0264	0.1203	0.1214	0.0101	0.0184	−0.1067
14.	69.	0.0686	0.2288	0.0032	0.0069	−0.0112	0.1344	0.1315	0.0201	0.0294	−0.0776
10.	46.	0.0719	0.2322	−0.0059	−0.0042	−0.0273	0.1296	0.1280	0.0080	0.0160	−0.1136
10.	47.	0.0633	0.2266	−0.0075	−0.0092	−0.0292	0.1245	0.1213	0.0055	0.0141	−0.1071
3.	9.	0.1801	0.2935	−0.0101	−0.0123	0.0031	0.2228	0.2247	0.0148	0.0204	−0.2972
3.	12.	0.1918	0.3000	−0.0097	−0.0110	0.0036	0.2338	0.2345	0.0170	0.0257	−0.3004
17.	101.	0.1727	0.2925	-0.0111	−0.0109	−0.0033	0.3592	0.2193	0.0136	0.0217	−0.2581
17.	98.	0.1602	0.2824	−0.0166	−0.0201	−0.0092	0.3223	0.2108	0.0032	0.0116	−0.2527
17.	99.	0.1451	0.2752	−0.0256	−0.0287	−0.0216	0.3418	0.2016	−0.0083	0.0037	−0.2588
10.	44.	0.1749	0.2996	−0.0020	−0.0053	0.0091	0.2272	0.2282	0.0208	0.0290	−0.2640
14.	70.	0.1584	0.2916	−0.0035	−0.0107	0.0065	0.2182	0.2176	0.0137	0.0228	−0.2506
14.	75.	0.1324	0.2648	−0.0219	−0.0269	−0.0182	0.1939	0.1858	−0.0061	0.0044	−0.2630
14.	76.	0.1321	0.2683	−0.0282	−0.0309	−0.0265	0.3277	0.1839	−0.0097	0.0006	−0.2737
14.	77.	0.1260	0.2577	−0.0277	−0.0350	−0.0268	0.3521	0.1794	−0.0132	−0.0032	−0.2600
17.	97.	0.1062	0.2551	−0.0008	−0.0041	−0.0124	0.3069	0.1653	0.0081	0.0184	−0.1940
17.	100.	0.0830	0.2349	−0.0311	−0.0295	−0.0441	0.2779	0.1457	−0.0127	−0.0020	−0.2200
14.	71.	0.1074	0.2508	−0.0201	−0.0198	−0.0218	0.1596	0.1637	0.0005	0.0100	−0.2804
14.	74.	0.1087	0.2506	−0.0210	−0.0239	−0.0246	0.1662	0.1653	−0.0047	0.0041	−0.2972
14.	79.	0.1267	0.2669	−0.0115	−0.0055	−0.0187	0.3328	0.1787	0.0103	0.0207	−0.2479
14.	81.	0.1169	0.2548	−0.0120	−0.0146	−0.0194	0.2621	0.1690	0.0001	0.0098	−0.2773

Table V. Pressure Coefficients for $l/h = 6.7$ Cavity at $\psi = 0°$

Run	Point	M_∞	$R \times 10^{-6}$	p_∞	$p_{t,\infty}$	q_∞	$T_{t,\infty}$	CP01	CP02	CP03	CP04	CP05	CP06	CP07	CP08	CP09	CP10	CP11
22.	161.	0.20	2.0	21.83	22.43	0.59	297.3	0.0056	0.0106	−0.0038	−0.0091	−0.0207	−0.0238	−0.0188	0.0019	0.0079	0.0046	0.0187
23.	164.	0.20	10.0	28.11	28.91	0.79	113.8	0.0162	0.0279	0.0122	0.0077	−0.0053	−0.0092	−0.0003	0.0273	0.0357	0.0262	0.0438
23.	165.	0.20	29.9	84.44	86.83	2.36	114.0	0.0129	0.0314	0.0124	0.0024	−0.0187	−0.0245	−0.0165	0.0248	0.0189	0.0207	0.0289
22.	159.	0.60	4.8	15.65	19.94	3.93	299.5	−0.0261	−0.0343	−0.0422	−0.0474	−0.0385	−0.0064	0.0403	0.0901	0.1300	0.1559	0.1747
22.	160.	0.60	10.2	33.65	42.92	8.48	299.4	−0.0253	−0.0335	−0.0427	−0.0493	−0.0409	−0.0086	0.0403	0.0979	0.1404	0.1701	0.1912
24.	198.	0.60	10.0	16.34	20.92	4.19	179.5	−0.0527	−0.0605	−0.0705	−0.0739	−0.0651	−0.0328	0.0158	0.0687	0.1125	0.1401	0.1595
24.	197.	0.60	30.0	49.19	62.87	12.51	179.1	−0.0443	−0.0518	−0.0630	−0.0694	−0.0620	−0.0285	0.0272	0.0861	0.1329	0.1633	0.1860
23.	170.	0.60	30.1	25.77	32.90	6.52	114.2	−0.0365	−0.0459	−0.0562	−0.0619	−0.0525	−0.0190	0.0332	0.0940	0.1392	0.1702	0.1931
23.	171.	0.60	80.2	68.15	86.83	17.09	113.2	−0.0394	−0.0476	−0.0583	−0.0614	−0.0499	−0.0102	0.0569	0.1190	0.1725	0.1943	0.2177
23.	172.	0.60	85.3	68.94	87.82	17.26	109.5	−0.0368	−0.0444	−0.0541	−0.0592	−0.0496	−0.0135	0.0415	0.1053	0.1631	0.1826	0.2055
22.	155.	0.80	6.2	14.40	21.94	6.44	300.1	−0.0273	−0.0352	−0.0422	−0.0495	−0.0479	−0.0274	0.0095	0.0547	0.0990	0.1294	0.1520
22.	156.	0.80	10.2	23.59	35.93	10.55	299.8	−0.0221	−0.0313	−0.0386	−0.0459	−0.0446	−0.0236	0.0153	0.0618	0.1052	0.1365	0.1567
25.	201.	0.80	10.6	15.03	22.93	6.75	208.9	−0.0331	−0.0400	−0.0478	−0.0535	−0.0533	−0.0339	0.0018	0.0433	0.0846	0.1157	0.1358
25.	202.	0.80	29.8	42.24	64.40	18.94	208.4	−0.0372	−0.0451	−0.0528	−0.0587	−0.0578	−0.0368	0.0019	0.0470	0.0928	0.1256	0.1495
23.	176.	0.80	30.1	17.62	26.91	7.93	113.2	−0.0182	−0.0254	−0.0336	−0.0407	−0.0371	−0.0124	0.0306	0.0821	0.1319	0.1658	0.1937
23.	175.	0.80	80.1	47.21	71.86	21.05	113.2	−0.0282	−0.0351	−0.0431	−0.0506	−0.0469	−0.0223	0.0216	0.0774	0.1281	0.1630	0.1889
23.	174.	0.80	90.3	52.73	80.34	23.56	112.7	−0.0232	−0.0306	−0.0376	−0.0451	−0.0463	−0.0290	0.0069	0.0529	0.0984	0.1315	0.1519
23.	173.	0.80	98.9	57.03	86.84	25.45	111.7	−0.0162	−0.0238	−0.0314	−0.0396	−0.0382	−0.0152	0.0262	0.0757	0.1248	0.1580	0.1817
25.	204.	0.91	12.6	15.13	25.92	8.80	209.1	−0.0248	−0.0326	−0.0379	−0.0440	−0.0483	−0.0360	−0.0080	0.0258	0.0619	0.0892	0.1057
25.	203.	0.91	30.0	35.93	61.39	20.80	208.5	−0.0182	−0.0263	−0.0315	−0.0380	−0.0423	−0.0287	0.0026	0.0417	0.0808	0.1118	0.1349
24.	185.	0.90	30.7	15.49	26.11	8.73	113.4	−0.0129	−0.0191	−0.0244	−0.0308	−0.0317	−0.0161	0.0138	0.0512	0.0896	0.1155	0.1354
24.	187.	0.90	79.5	39.91	67.38	22.54	113.3	−0.0478	−0.0542	−0.0606	−0.0679	−0.0697	−0.0554	−0.0233	0.0190	0.0588	0.0878	0.1113
24.	188.	0.90	89.6	44.94	75.86	25.38	113.3	−0.0185	−0.0250	−0.0316	−0.0397	−0.0421	−0.0256	0.0082	0.0496	0.0904	0.1240	0.1456
24.	189.	0.90	99.5	50.00	84.34	28.20	113.4	−0.0234	−0.0305	−0.0360	−0.0428	−0.0451	−0.0329	0.0000	0.0400	0.0777	0.1095	0.1306

Table V. Concluded

Run	Point	CP12	CP13	CP14	CP15	CP16	CP17	CP18	CP19	CP20	CP21
22.	161.	0.0463	0.1508	0.0226	0.0058	−0.0076	0.2446	0.0880	0.0086	0.0079	−0.0881
23.	164.	0.0749	0.1716	0.0291	0.0238	−0.0037	0.2908	0.0988	0.0247	0.0272	−0.0773
23.	165.	0.0794	0.1776	0.0332	0.0245	−0.0085	0.2976	0.1148	0.0177	0.0230	−0.0905
22.	159.	0.1767	0.2508	−0.0284	−0.0281	0.0095	0.4189	0.1477	−0.0067	−0.0102	−0.2819
22.	160.	0.2074	0.2659	−0.0259	−0.0272	0.0129	0.4314	0.1748	−0.0048	−0.0050	−0.3022
24.	198.	0.1700	0.2429	−0.0432	−0.0546	−0.0048	0.3953	0.1446	−0.0300	−0.0315	−0.3322
24.	197.	0.1959	0.2699	−0.0426	−0.0458	−0.0009	0.4198	0.1648	−0.0236	−0.0233	−0.3419
23.	170.	0.2048	0.2723	−0.0209	−0.0389	0.0230	0.4527	0.1797	−0.0118	−0.0136	−0.3313
23.	171.	0.2376	0.2938	−0.0387	−0.0415	0.0178	0.4587	0.1954	−0.0143	−0.0165	−0.3669
23.	172.	0.2251	0.2929	−0.0351	−0.0383	0.0166	0.4453	0.1912	−0.0131	−0.0146	−0.3418
22.	155.	0.1617	0.2457	−0.0369	−0.0284	−0.0213	0.3859	0.1380	−0.0141	−0.0165	−0.2950
22.	156.	0.1722	0.2566	−0.0197	−0.0257	−0.0015	0.3969	0.1559	−0.0082	−0.0091	−0.2902
25.	201.	0.1479	0.2424	−0.0295	−0.0340	−0.0139	0.3593	0.1327	−0.0184	−0.0205	−0.3120
25.	202.	0.1660	0.2591	−0.0362	−0.0390	−0.0202	0.3758	0.1538	−0.0236	−0.0244	−0.3401
23.	176.	0.2173	0.2909	−0.0170	−0.0187	0.0080	0.4428	0.1891	−0.0008	−0.0017	−0.3378
23.	175.	0.2168	0.2952	−0.0237	−0.0297	0.0011	0.4182	0.1861	−0.0102	−0.0133	−0.3634
23.	174.	0.1655	0.2754	−0.0031	−0.0250	0.0168	0.3905	0.1705	−0.0067	−0.0105	−0.3135
23.	173.	0.1962	0.2917	−0.0097	−0.0177	0.0117	0.4078	0.1789	−0.0009	−0.0033	−0.3221
25.	204.	0.1133	0.2271	−0.0174	−0.0273	−0.0170	0.3130	0.1195	−0.0169	−0.0158	−0.2525
25.	203.	0.1489	0.2564	−0.0215	−0.0194	−0.0185	0.3353	0.1438	−0.0098	−0.0073	−0.2721
24.	185.	0.1473	0.2565	−0.0122	−0.0137	−0.0055	0.3562	0.1444	−0.0012	−0.0007	−0.2505
24.	187.	0.1248	0.2447	−0.0496	−0.0490	−0.0431	0.3194	0.1234	−0.0370	−0.0377	−0.3091
24.	188.	0.1570	0.2691	−0.0195	−0.0196	−0.0102	0.3486	0.1492	−0.0068	−0.0081	−0.2892
24.	189.	0.1389	0.2598	−0.0235	−0.0246	−0.0175	0.3377	0.1377	−0.0139	−0.0146	−0.2559

Table VI. Pressure Coefficients for $l/h = 12.67$ Cavity at $\psi = 0°$

Run	Point	M_∞	$R \times 10^{-6}$	p_∞	$p_{t,\infty}$	q_∞	$T_{t,\infty}$	CP01	CP02	CP03	CP04	CP05	CP06	CP07	CP08	CP09	CP10	CP11
21.	148.	0.60	4.3	15.21	19.43	3.86	319.0	−0.1097	−0.1323	−0.0866	0.0387	0.1353	0.1669	0.1673	0.1731	0.1937	0.2387	0.3073
21.	149.	0.60	10.2	36.32	46.32	9.15	318.8	−0.1059	−0.1282	−0.0874	0.0389	0.1417	0.1767	0.1770	0.1844	0.2046	0.2515	0.3231
19.	135.	0.60	10.0	16.58	21.14	4.17	180.0	−0.1214	−0.1438	−0.1003	0.0299	0.1348	0.1672	0.1670	0.1708	0.1916	0.2382	0.3129
19.	137.	0.60	30.3	50.23	64.05	12.65	179.6	−0.1207	−0.1418	−0.1015	0.0282	0.1381	0.1733	0.1727	0.1792	0.1998	0.2493	0.3281
18.	106.	0.60	30.1	25.81	32.89	6.48	114.1	−0.1179	−0.1374	−0.0930	0.0383	0.1426	0.1731	0.1719	0.1795	0.2007	0.2478	0.3272
18.	107.	0.60	79.3	68.10	86.77	17.08	114.0	−0.1272	−0.1467	−0.0935	0.0455	0.1501	0.1772	0.1727	0.1801	0.2004	0.2516	0.3355
18.	108.	0.60	85.2	68.88	87.77	17.28	109.6	−0.1201	−0.1391	−0.0902	0.0488	0.1561	0.1831	0.1779	0.1849	0.2052	0.2566	0.3402
21.	151.	0.80	5.0	12.01	18.32	5.39	309.7	−0.1088	−0.1260	−0.1159	−0.0366	0.0637	0.1370	0.1686	0.1866	0.2111	0.2541	0.3131
21.	150.	0.80	10.1	24.19	36.85	10.82	308.8	−0.1054	−0.1212	−0.1126	−0.0342	0.0678	0.1445	0.1789	0.1991	0.2229	0.2665	0.3286
20.	139.	0.80	10.2	14.66	22.35	6.57	210.7	−0.1118	−0.1294	−0.1169	−0.0311	0.0764	0.1497	0.1788	0.1946	0.2189	0.2645	0.3294
20.	138.	0.80	30.1	40.10	61.26	18.07	199.4	−0.1168	−0.1332	−0.1270	−0.0493	0.0583	0.1412	0.1790	0.2005	0.2257	0.2738	0.3408
18.	119.	0.81	30.7	18.21	27.90	8.26	114.5	−0.1116	−0.1264	−0.1198	−0.0439	0.0641	0.1457	0.1820	0.2024	0.2274	0.2737	0.3413
18.	118.	0.80	80.4	48.26	73.41	21.49	114.6	−0.1207	−0.1356	−0.1283	−0.0470	0.0651	0.1492	0.1845	0.2048	0.2300	0.2794	0.3513
18.	117.	0.80	90.0	54.12	82.29	24.07	114.6	−0.1186	−0.1325	−0.1262	−0.0454	0.0665	0.1500	0.1863	0.2078	0.2327	0.2824	0.3541
18.	116.	0.80	98.7	57.75	87.78	25.66	112.6	−0.1160	−0.1308	−0.1232	−0.0411	0.0737	0.1559	0.1899	0.2099	0.2346	0.2848	0.3570
20.	142.	0.91	12.5	15.13	25.81	8.73	210.1	−0.0698	−0.0836	−0.0832	−0.0342	0.0430	0.1240	0.1813	0.2202	0.2527	0.2935	0.3414
20.	143.	0.91	30.0	36.36	61.85	20.86	209.6	−0.0933	−0.1050	−0.1066	−0.0631	0.0132	0.0978	0.1624	0.2087	0.2439	0.2867	0.3367
18.	120.	0.91	30.1	15.17	25.90	8.77	114.6	−0.0902	−0.1011	−0.1030	−0.0594	0.0167	0.1009	0.1629	0.2086	0.2435	0.2846	0.3345
18.	121.	0.90	80.1	40.76	68.82	23.03	114.5	−0.0779	−0.0892	−0.0909	−0.0460	0.0341	0.1203	0.1848	0.2305	0.2657	0.3098	0.3621
18.	122.	0.90	90.0	45.66	77.32	25.96	114.5	−0.0798	−0.0905	−0.0924	−0.0470	0.0336	0.1209	0.1851	0.2310	0.2656	0.3102	0.3631
18.	123.	0.90	100.4	50.96	86.30	28.97	114.5	−0.0810	−0.0922	−0.0939	−0.0488	0.0287	0.1151	0.1805	0.2282	0.2635	0.3084	0.3596

Table VI. Concluded

Run	Point	CP12	CP13	CP14	CP15	CP16	CP17	CP18	CP19	CP20	CP21
21.	148.	0.3863	0.3498	−0.1125	−0.1142	0.1696	0.5085	0.4080	−0.0480	−0.0764	−0.6149
21.	149.	0.4099	0.3752	−0.0951	−0.1119	0.1955	0.5336	0.4353	−0.0413	−0.0679	−0.6347
19.	135.	0.4015	0.3673	−0.1183	−0.1263	0.1703	0.5336	0.4217	−0.0559	−0.0832	−0.6615
19.	137.	0.4237	0.4147	−0.1174	−0.1251	0.1794	0.5549	0.4480	−0.0517	−0.0789	−0.6842
18.	106.	0.4224	0.3995	−0.1222	−0.1189	0.1835	0.5813	0.4397	−0.0491	−0.0753	−0.6641
18.	107.	0.4446	0.4329	−0.1325	−0.1282	0.1820	0.5962	0.4616	−0.0551	−0.0835	−0.7120
18.	108.	0.4476	0.4383	−0.1205	−0.1215	0.1928	0.5988	0.4658	−0.0478	−0.0764	−0.7042
21.	151.	0.3745	0.3494	−0.1110	−0.1143	0.1629	0.4845	0.3947	−0.0554	−0.0814	−0.6251
21.	150.	0.3942	0.3659	−0.1122	−0.1102	0.1671	0.4958	0.4149	−0.0513	−0.0762	−0.6384
20.	139.	0.3981	0.3712	−0.1166	−0.1173	0.1684	0.5137	0.4182	−0.0524	−0.0795	−0.6587
20.	138.	0.4129	0.4005	−0.1096	−0.1238	0.1778	0.5338	0.4364	−0.0549	−0.0825	−0.6753
18.	119.	0.4111	0.4012	−0.1093	−0.1169	0.1749	0.5282	0.4327	−0.0517	−0.0779	−0.6650
18.	118.	0.4289	0.4220	−0.1166	−0.1254	0.1802	0.5454	0.4491	−0.0586	−0.0871	−0.7034
18.	117.	0.4333	0.4247	−0.1162	−0.1232	0.1805	0.5491	0.4523	−0.0579	−0.0856	−0.6995
18.	116.	0.4368	0.4302	−0.1193	−0.1199	0.1799	0.5516	0.4570	−0.0558	−0.0825	−0.6981
20.	142.	0.3921	0.3752	−0.0643	−0.0783	0.1711	0.4993	0.4185	−0.0230	−0.0449	−0.5709
20.	143.	0.3895	0.3772	−0.0856	−0.1007	0.1504	0.4993	0.4135	−0.0438	−0.0671	−0.6130
18.	120.	0.3868	0.3719	−0.0774	−0.0968	0.1562	0.5003	0.4071	−0.0424	−0.0648	−0.6222
18.	121.	0.4182	0.4124	−0.0746	−0.0847	0.1658	0.5280	0.4371	−0.0315	−0.0549	−0.6031
18.	122.	0.4208	0.4156	−0.0750	−0.0864	0.1666	0.5326	0.4397	−0.0319	−0.0560	−0.6127
18.	123.	0.4157	0.4109	−0.0758	−0.0903	0.1635	0.5203	0.4362	−0.0345	−0.0581	−0.6070

Table VII. Pressure Coefficients for $l/h = 20.0$ Cavity at $\psi = 0°$

Run	Point	M_∞	$R \times 10^{-6}$	p_∞	$p_{t,\infty}$	q_∞	$T_{t,\infty}$	CP01	CP02	CP03	CP04	CP05	CP06	CP07	CP08	CP09	CP10	CP11
27.	215.	0.60	4.9	15.84	20.24	4.03	299.4	−0.1258	−0.0616	0.0868	0.1217	0.1025	0.0825	0.0734	0.0775	0.0944	0.1310	0.2009
27.	214.	0.60	10.0	32.84	41.93	8.31	299.3	−0.1245	−0.0616	0.0934	0.1302	0.1083	0.0871	0.0780	0.0848	0.1008	0.1380	0.2111
29.	241.	0.60	9.9	16.40	20.93	4.14	179.9	−0.1420	−0.0753	0.0815	0.1191	0.0969	0.0739	0.0645	0.0684	0.0853	0.1214	0.1959
29.	240.	0.60	30.1	49.66	63.38	12.55	179.6	−0.1401	−0.0706	0.0925	0.1288	0.1041	0.0789	0.0696	0.0773	0.0936	0.1321	0.2096
28.	237.	0.60	30.0	25.80	32.92	6.51	114.6	−0.1300	−0.0640	0.0964	0.1355	0.1128	0.0894	0.0797	0.0864	0.1029	0.1410	0.2173
28.	238.	0.60	79.8	65.22	83.05	16.31	110.2	−0.1357	−0.0675	0.1023	0.1387	0.1126	0.0868	0.0765	0.0857	0.1016	0.1416	0.2200
28.	239.	0.60	85.4	68.99	87.84	17.24	109.4	−0.1303	−0.0632	0.1071	0.1435	0.1169	0.0903	0.0796	0.0886	0.1043	0.1443	0.2224
27.	217.	0.80	6.2	14.88	22.74	6.71	309.0	−0.1380	−0.1071	0.0354	0.1104	0.1110	0.0922	0.0810	0.0847	0.1044	0.1470	0.2251
27.	218.	0.80	9.9	22.88	34.91	10.28	299.7	−0.1361	−0.1049	0.0382	0.1153	0.1153	0.0957	0.0841	0.0889	0.1082	0.1513	0.2311
30.	242.	0.80	10.4	14.87	22.74	6.72	210.9	−0.1424	−0.1097	0.0346	0.1145	0.1146	0.0934	0.0812	0.0841	0.1039	0.1479	0.2291
30.	243.	0.80	30.1	43.15	65.91	19.44	210.3	−0.1357	−0.1071	0.0395	0.1243	0.1256	0.1036	0.0909	0.0969	0.1165	0.1622	0.2458
28.	222.	0.80	29.9	17.61	26.92	7.94	113.6	−0.1367	−0.1087	0.0377	0.1220	0.1224	0.0993	0.0853	0.0894	0.1093	0.1542	0.2398
28.	221.	0.80	80.0	47.35	72.11	21.14	113.6	−0.1402	−0.1107	0.0427	0.1288	0.1257	0.0999	0.0843	0.0904	0.1100	0.1570	0.2462
28.	220.	0.80	90.2	51.97	79.15	23.21	111.7	−0.1376	−0.1058	0.0497	0.1315	0.1275	0.1017	0.0860	0.0925	0.1120	0.1592	0.2480
28.	219.	0.80	100.1	57.69	87.85	25.74	111.7	−0.1321	−0.1016	0.0526	0.1366	0.1326	0.1068	0.0910	0.0978	0.1173	0.1650	0.2534
30.	245.	0.91	12.1	14.81	25.23	8.52	211.1	−0.1156	−0.1015	0.0189	0.1174	0.1449	0.1362	0.1264	0.1307	0.1525	0.1988	0.2782
30.	244.	0.91	30.1	36.45	62.39	21.18	210.5	−0.1286	−0.1159	0.0046	0.1092	0.1396	0.1295	0.1177	0.1224	0.1439	0.1930	0.2786
28.	223.	0.89	30.0	15.49	25.92	8.59	114.7	−0.1355	−0.1207	0.0043	0.1070	0.1321	0.1188	0.1060	0.1108	0.1334	0.1817	0.2674
28.	224.	0.90	79.9	40.93	68.89	22.98	114.6	−0.1410	−0.1274	−0.0008	0.1073	0.1360	0.1221	0.1077	0.1141	0.1366	0.1880	0.2777
28.	226.	0.90	90.0	45.78	77.37	25.91	114.6	−0.1479	−0.1347	−0.0117	0.0976	0.1322	0.1220	0.1083	0.1149	0.1372	0.1888	0.2778
28.	229.	0.90	100.0	51.16	86.34	28.88	114.7	−0.1458	−0.1324	−0.0083	0.1026	0.1355	0.1235	0.1093	0.1157	0.1380	0.1896	0.2795

Table VII. Concluded

Run	Point	CP12	CP13	CP14	CP15	CP16	CP17	CP18	CP19	CP20	CP21
27.	215.	0.3156	0.3727	−0.1280	−0.1325	0.0819	0.3711	0.3681	−0.0613	−0.0934	−0.4938
27.	214.	0.3333	0.3946	−0.1312	−0.1318	0.0833	0.3886	0.3880	−0.0626	−0.0958	−0.5037
29.	241.	0.3206	0.3854	−0.1424	−0.1478	0.0701	0.3750	0.3766	−0.0752	−0.1104	−0.5397
29.	240.	0.3458	0.4217	−0.1399	−0.1461	0.0769	0.4033	0.4076	−0.0779	−0.1157	−0.5627
28.	237.	0.3501	0.4244	−0.1270	−0.1367	0.0880	0.4050	0.4097	−0.0677	−0.1052	−0.5337
28.	238.	0.3638	0.4494	−0.1394	−0.1410	0.0793	0.4173	0.4307	−0.0782	−0.1184	−0.5643
28.	239.	0.3671	0.4542	−0.1300	−0.1358	0.0859	0.4232	0.4349	−0.0727	−0.1128	−0.5634
27.	217.	0.3373	0.3838	−0.1450	−0.1451	0.0863	0.3833	0.3843	−0.0741	−0.1091	−0.5561
27.	218.	0.3476	0.3974	−0.1434	−0.1436	0.0894	0.3948	0.3963	−0.0735	−0.1086	−0.5608
30.	242.	0.3489	0.4036	−0.1417	−0.1498	0.0896	0.3960	0.3997	−0.0753	−0.1128	−0.5808
30.	243.	0.3740	0.4374	−0.1353	−0.1429	0.1009	0.4249	0.4274	−0.0750	−0.1146	−0.5837
28.	222.	0.3679	0.4286	−0.1322	−0.1416	0.0979	0.4146	0.4203	−0.0728	−0.1133	−0.5976
28.	221.	0.3857	0.4539	−0.1408	−0.1450	0.0948	0.4315	0.4422	−0.0807	−0.1250	−0.6304
28.	220.	0.3884	0.4558	−0.1429	−0.1427	0.0926	0.4323	0.4450	−0.0780	−0.1226	−0.6244
28.	219.	0.3940	0.4632	−0.1321	−0.1373	0.1022	0.4404	0.4528	−0.0712	−0.1163	−0.6199
30.	245.	0.3845	0.4306	−0.1169	−0.1245	0.1339	0.4271	0.4307	−0.0528	−0.0900	−0.5533
30.	244.	0.3963	0.4499	−0.1292	−0.1359	0.1269	0.4408	0.4434	−0.0685	−0.1099	−0.6186
28.	223.	0.3836	0.4362	−0.1341	−0.1408	0.1154	0.4244	0.4292	−0.0723	−0.1138	−0.5848
28.	224.	0.4029	0.4614	−0.1400	−0.1466	0.1181	0.4420	0.4525	−0.0824	−0.1279	−0.6292
28.	226.	0.4022	0.4622	−0.1463	−0.1535	0.1187	0.4412	0.4544	−0.0888	−0.1352	−0.6424
28.	229.	0.4058	0.4660	−0.1433	−0.1501	0.1196	0.4428	0.4560	−0.0870	−0.1332	−0.6472

Table VIII. Pressure Coefficients for $l/h = 4.4$ Cavity at $\psi = 15°$

Run	Point	M_∞	$R \times 10^{-6}$	p_∞	$p_{t,\infty}$	q_∞	$T_{t,\infty}$	CP01	CP02	CP03	CP04	CP05	CP06	CP07	CP08	CP09	CP10	CP11
4.	22.	0.20	2.1	22.19	22.81	0.62	297.1	−0.0417	−0.0290	−0.0457	−0.0337	−0.0360	−0.0215	0.0098	0.0553	0.0868	0.1248	0.1879
11.	54.	0.20	9.3	22.72	23.36	0.63	103.4	−0.0530	−0.0334	−0.0405	−0.0336	−0.0334	−0.0219	0.0168	0.0794	0.1276	0.1727	0.2504
11.	53.	0.20	27.9	68.02	69.94	1.91	103.3	−0.0998	−0.0709	−0.0821	−0.0769	−0.0805	−0.0596	0.0126	0.1194	0.1773	0.2519	0.3446
4.	19.	0.60	4.0	14.23	18.17	3.61	319.0	−0.0747	−0.0888	−0.0844	−0.0714	−0.0483	−0.0044	0.0534	0.1148	0.1672	0.2254	0.2877
4.	24.	0.60	4.0	14.23	18.17	3.60	319.2	−0.0868	−0.1038	−0.0987	−0.0831	−0.0564	−0.0086	0.0521	0.1129	0.1686	0.2283	0.2911
12.	57.	0.60	10.0	16.59	21.14	4.16	179.9	−0.1025	−0.1132	−0.1067	−0.0950	−0.0752	−0.0357	0.0193	0.0808	0.1331	0.1935	0.2566
11.	50.	0.60	30.1	22.51	28.68	5.64	103.9	−0.1001	−0.1131	−0.1039	−0.0885	−0.0609	−0.0098	0.0557	0.1283	0.1845	0.2493	0.3214
11.	51.	0.60	80.2	59.76	76.21	15.03	104.0	−0.1121	−0.1234	−0.1146	−0.0951	−0.0612	−0.0050	0.0711	0.1529	0.2126	0.2791	0.3519
11.	52.	0.60	90.1	67.69	86.08	16.82	104.0	−0.1180	−0.1312	−0.1207	−0.0978	−0.0588	0.0005	0.0816	0.1638	0.2200	0.2859	0.3604
4.	20.	0.77	5.8	14.13	20.86	5.82	299.1	−0.1124	−0.1316	−0.1296	−0.0964	−0.0246	0.0591	0.1297	0.1872	0.2378	0.2970	0.3779
4.	23.	0.79	10.2	23.59	35.53	10.25	295.7	−0.0889	−0.1003	−0.0958	−0.0812	−0.0500	0.0026	0.0631	0.1255	0.1800	0.2397	0.3077
16.	92.	0.80	10.1	14.91	22.73	6.68	214.6	−0.0898	−0.1003	−0.0956	−0.0831	−0.0577	−0.0110	0.0454	0.1043	0.1572	0.2145	0.2816
15.	87.	0.80	30.1	17.38	26.51	7.80	111.8	−0.1050	−0.1136	−0.1083	−0.0963	−0.0711	−0.0254	0.0345	0.0988	0.1558	0.2127	0.2797
15.	84.	0.80	80.0	47.55	72.33	21.17	113.8	−0.0973	−0.1085	−0.1037	−0.0902	−0.0617	−0.0121	0.0544	0.1294	0.1850	0.2442	0.3148
15.	82.	0.80	90.1	53.66	81.60	23.87	113.9	−0.0994	−0.1100	−0.1042	−0.0904	−0.0629	−0.0129	0.0549	0.1259	0.1838	0.2454	0.3164
15.	86.	0.80	99.6	57.76	87.78	25.64	111.8	−0.0957	−0.1062	−0.0985	−0.0862	−0.0608	−0.0143	0.0494	0.1149	0.1714	0.2309	0.2996
15.	88.	0.92	29.1	14.50	24.93	8.50	114.4	−0.0716	−0.0731	−0.0678	−0.0593	−0.0436	−0.0136	0.0281	0.0793	0.1226	0.1670	0.2316
15.	85.	0.91	80.3	40.14	68.33	23.06	113.8	−0.0736	−0.0752	−0.0699	−0.0614	−0.0460	−0.0150	0.0326	0.0903	0.1379	0.1862	0.2517
15.	83.	0.91	90.1	44.98	76.81	26.01	113.9	−0.0685	−0.0695	−0.0640	−0.0555	−0.0403	−0.0088	0.0371	0.0928	0.1399	0.1898	0.2547

Table VIII. Concluded

Run	Point	CP12	CP13	CP14	CP15	CP16	CP17	CP18	CP19	CP20	CP21
4.	22.	0.2280	0.3058	−0.0267	−0.0484	0.0371	0.2806	0.2706	−0.0015	−0.0193	−0.4549
11.	54.	0.2991	0.3658	−0.0136	−0.0423	0.0339	0.3159	0.3170	0.0005	−0.0141	−0.5405
11.	53.	0.4124	0.4245	−0.0828	−0.0853	0.0001	0.3636	0.4010	−0.0333	−0.0509	−0.6870
4.	19.	0.3280	0.3720	−0.0828	−0.0773	0.1048	0.3237	0.3535	−0.0131	−0.0267	−0.5850
4.	24.	0.3331	0.3736	−0.1020	−0.0906	0.1018	0.3238	0.3593	−0.0218	−0.0367	−0.6230
12.	57.	0.3009	0.3538	−0.1117	−0.1023	0.0920	0.3258	0.3387	−0.0395	−0.0483	−0.6165
11.	50.	0.3733	0.4154	−0.1060	−0.1001	0.1155	0.3663	0.4018	−0.0271	−0.0358	−0.6604
11.	51.	0.4179	0.4516	−0.1145	−0.1122	0.1268	0.3935	0.4425	−0.0309	−0.0412	−0.6972
11.	52.	0.4291	0.4700	−0.1239	−0.1164	0.1306	0.4006	0.4536	−0.0340	−0.0429	−0.7083
4.	20.	0.4537	0.4861	−0.1222	−0.1139	0.1810	0.4349	0.4902	−0.0189	−0.0369	−0.7069
4.	23.	0.3705	0.4121	−0.0958	−0.0901	0.1221	0.3739	0.4102	−0.0175	−0.0301	−0.6641
16.	92.	0.3400	0.3856	−0.0953	−0.0905	0.0991	0.3580	0.3759	−0.0248	−0.0347	−0.6141
15.	87.	0.3374	0.3844	−0.0964	−0.1047	0.1010	0.3530	0.3727	−0.0353	−0.0446	−0.6532
15.	84.	0.3751	0.4163	−0.1005	−0.0992	0.1045	0.3752	0.3999	−0.0270	−0.0355	−0.6615
15.	82.	0.3738	0.4142	−0.1008	−0.0991	0.1147	0.3780	0.3987	−0.0276	−0.0362	−0.6785
15.	86.	0.3653	0.4118	−0.0974	−0.0954	0.1130	0.3699	0.3954	−0.0268	−0.0357	−0.6479
15.	88.	0.2964	0.3607	−0.0680	−0.0689	0.0652	0.2890	0.3304	−0.0175	−0.0235	−0.5925
15.	85.	0.3194	0.3757	−0.0691	−0.0719	0.0735	0.3092	0.3481	−0.0169	−0.0245	−0.6316
15.	83.	0.3226	0.3856	−0.0641	−0.0665	0.0799	0.3227	0.3535	−0.0107	−0.0184	−0.6605

Table IX. Pressure Coefficients for $l/h = 6.7$ Cavity at $\psi = 15°$

Run	Point	M_∞	$R \times 10^{-6}$	p_∞	$p_{t,\infty}$	q_∞	$T_{t,\infty}$	CP01	CP02	CP03	CP04	CP05	CP06	CP07	CP08	CP09	CP10	CP11
22.	162.	0.20	2.0	21.84	22.43	0.59	297.4	−0.1247	−0.1109	−0.1107	−0.0636	0.0024	0.0829	0.1391	0.1911	0.2091	0.2250	0.2984
23.	163.	0.20	10.0	28.13	28.93	0.79	114.0	−0.1246	−0.1032	−0.1017	−0.0450	0.0318	0.1068	0.1624	0.2168	0.2340	0.2413	0.3135
23.	166.	0.20	29.8	84.44	86.83	2.36	114.1	−0.1571	−0.1258	−0.1165	−0.0457	0.0377	0.1223	0.1786	0.2461	0.2514	0.2800	0.3457
22.	158.	0.60	4.7	15.62	19.91	3.93	299.8	−0.1116	−0.1177	−0.1070	−0.0661	−0.0024	0.0700	0.1300	0.1759	0.2042	0.2337	0.2946
24.	199.	0.60	10.0	16.34	20.93	4.19	179.5	−0.1284	−0.1310	−0.1229	−0.0831	−0.0199	0.0555	0.1185	0.1696	0.2000	0.2282	0.2912
23.	169.	0.60	30.1	25.80	32.93	6.51	114.3	−0.1310	−0.1297	−0.1185	−0.0765	−0.0097	0.0686	0.1325	0.1847	0.2137	0.2402	0.3027
23.	168.	0.60	79.9	68.99	87.83	17.24	114.2	−0.1314	−0.1310	−0.1197	−0.0754	−0.0059	0.0780	0.1427	0.2006	0.2262	0.2545	0.3174
23.	167.	0.60	84.4	68.97	87.82	17.24	110.2	−0.1203	−0.1195	−0.1064	−0.0623	0.0077	0.0897	0.1522	0.2096	0.2351	0.2627	0.3234
22.	157.	0.80	6.5	15.10	22.93	6.70	300.4	−0.0943	−0.0961	−0.0900	−0.0674	−0.0314	0.0215	0.0791	0.1349	0.1762	0.2157	0.2751
25.	200.	0.80	10.6	15.04	22.94	6.75	209.0	−0.1005	−0.1003	−0.0954	−0.0724	−0.0363	0.0160	0.0757	0.1350	0.1785	0.2176	0.2784
23.	177.	0.80	30.1	17.61	26.91	7.94	113.2	−0.0944	−0.0944	−0.0879	−0.0633	−0.0245	0.0321	0.0950	0.1577	0.2015	0.2389	0.2987
23.	178.	0.80	80.0	46.99	71.62	21.03	113.1	−0.1036	−0.1025	−0.0970	−0.0717	−0.0315	0.0270	0.0913	0.1589	0.2019	0.2413	0.3008
23.	179.	0.80	90.3	53.10	80.85	23.69	113.1	−0.1115	−0.1103	−0.1050	−0.0813	−0.0427	0.0141	0.0776	0.1449	0.1889	0.2315	0.2916
23.	180.	0.80	98.7	57.78	87.83	25.67	112.6	−0.1073	−0.1050	−0.0996	−0.0742	−0.0340	0.0256	0.0903	0.1578	0.2012	0.2407	0.3023
25.	205.	0.90	12.6	15.25	25.92	8.73	208.9	−0.0886	−0.0900	−0.0874	−0.0726	−0.0525	−0.0209	0.0205	0.0680	0.1112	0.1486	0.1943
24.	184.	0.89	30.8	15.52	26.11	8.70	113.3	−0.0911	−0.0921	−0.0894	−0.0745	−0.0513	−0.0169	0.0287	0.0823	0.1282	0.1695	0.2191
24.	183.	0.91	80.3	39.84	67.86	22.92	113.2	−0.0772	−0.0772	−0.0744	−0.0596	−0.0370	−0.0012	0.0443	0.1012	0.1478	0.1894	0.2389
24.	182.	0.89	90.1	45.41	76.10	25.27	113.2	−0.0849	−0.0838	−0.0809	−0.0649	−0.0422	−0.0047	0.0435	0.1027	0.1486	0.1905	0.2431
24.	181.	0.88	99.8	51.06	84.84	27.90	113.3	−0.0988	−0.0990	−0.0953	−0.0784	−0.0544	−0.0152	0.0349	0.0962	0.1439	0.1878	0.2427

Table IX. Concluded

Run	Point	CP12	CP13	CP14	CP15	CP16	CP17	CP18	CP19	CP20	CP21
22.	162.	0.4689	0.4643	−0.1116	−0.1168	0.2333	0.6580	0.5213	−0.0406	−0.0704	−0.7124
23.	163.	0.5149	0.4513	−0.0933	−0.1061	0.2718	0.6885	0.5543	−0.0255	−0.0540	−0.6743
23.	166.	0.5689	0.4876	−0.1284	−0.1320	0.2948	0.7139	0.5947	−0.0391	−0.0691	−0.7327
22.	158.	0.4281	0.4465	−0.1114	−0.1099	0.2030	0.6175	0.4824	−0.0354	−0.0580	−0.6878
24.	199.	0.4322	0.4514	−0.1203	−0.1257	0.1951	0.6183	0.4887	−0.0477	−0.0694	−0.7154
23.	169.	0.4608	0.4979	−0.1195	−0.1265	0.2154	0.6530	0.5241	−0.0414	−0.0640	−0.7092
23.	168.	0.4864	0.5374	−0.1253	−0.1267	0.2270	0.6665	0.5475	−0.0401	−0.0640	−0.7086
23.	167.	0.4962	0.5488	−0.1126	−0.1147	0.2380	0.6748	0.5577	−0.0290	−0.0535	−0.6931
22.	157.	0.3565	0.3741	−0.0918	−0.0938	0.1304	0.5767	0.3957	−0.0334	−0.0522	−0.6829
25.	200.	0.3610	0.3827	−0.0965	−0.0990	0.1287	0.5667	0.3997	−0.0379	−0.0561	−0.6966
23.	177.	0.3957	0.4261	−0.0846	−0.0927	0.1498	0.5968	0.4393	−0.0269	−0.0459	−0.6997
23.	178.	0.4121	0.4555	−0.0942	−0.1023	0.1549	0.6015	0.4650	−0.0330	−0.0546	−0.7368
23.	179.	0.3984	0.4454	−0.1006	−0.1099	0.1390	0.5862	0.4501	−0.0432	−0.0635	−0.7294
23.	180.	0.4142	0.4540	−0.0969	−0.1047	0.1494	0.5957	0.4590	−0.0361	−0.0571	−0.7373
25.	205.	0.2411	0.2828	−0.0803	−0.0900	0.0575	0.4661	0.2624	−0.0458	−0.0578	−0.6180
24.	184.	0.2717	0.3107	−0.0750	−0.0917	0.0739	0.4995	0.2916	−0.0394	−0.0548	−0.6538
24.	183.	0.2990	0.3395	−0.0636	−0.0773	0.0852	0.5057	0.3188	−0.0284	−0.0441	−0.6606
24.	182.	0.3064	0.3412	−0.0737	−0.0846	0.0876	0.5083	0.3243	−0.0327	−0.0489	−0.6573
24.	181.	0.3126	0.3465	−0.0821	−0.1000	0.0835	0.5174	0.3341	−0.0425	−0.0606	−0.7022

Table X. Pressure Coefficients for $l/h = 12.67$ Cavity at $\psi = 15°$

Run	Point	M_∞	$R \times 10^{-6}$	p_∞	$p_{t,\infty}$	q_∞	$T_{t,\infty}$	CP01	CP02	CP03	CP04	CP05	CP06	CP07	CP08	CP09	CP10	CP11
21.	147.	0.60	4.3	15.23	19.43	3.83	319.3	−0.1402	−0.1245	−0.0088	0.1010	0.1418	0.1468	0.1433	0.1445	0.1520	0.1732	0.2100
19.	136.	0.60	10.0	16.57	21.12	4.17	180.0	−0.1506	−0.1310	−0.0108	0.1022	0.1445	0.1484	0.1441	0.1464	0.1532	0.1734	0.2129
18.	111.	0.60	30.2	25.74	32.90	6.54	114.0	−0.1553	−0.1279	−0.0038	0.1049	0.1482	0.1532	0.1482	0.1527	0.1586	0.1755	0.2126
18.	110.	0.60	76.5	65.72	83.77	16.50	114.1	−0.1615	−0.1269	0.0079	0.1159	0.1562	0.1581	0.1508	0.1578	0.1622	0.1810	0.2173
18.	109.	0.60	85.2	68.89	87.77	17.26	109.5	−0.1602	−0.1244	0.0087	0.1148	0.1554	0.1586	0.1516	0.1586	0.1628	0.1818	0.2174
21.	146.	0.80	6.5	15.70	23.92	7.03	309.6	−0.1259	−0.1217	−0.0368	0.0713	0.1340	0.1562	0.1621	0.1687	0.1785	0.1979	0.2303
20.	140.	0.80	10.4	14.91	22.72	6.68	210.0	−0.1436	−0.1386	−0.0581	0.0510	0.1190	0.1453	0.1519	0.1604	0.1709	0.1910	0.2224
18.	112.	0.80	31.7	19.04	28.89	8.43	114.2	−0.1377	−0.1255	−0.0415	0.0661	0.1339	0.1582	0.1638	0.1730	0.1824	0.1987	0.2276
18.	113.	0.80	79.8	47.72	72.57	21.23	114.2	−0.1437	−0.1297	−0.0413	0.0687	0.1369	0.1631	0.1676	0.1798	0.1889	0.2069	0.2350
18.	114.	0.80	89.8	53.70	81.63	23.86	114.2	−0.1450	−0.1306	−0.0414	0.0682	0.1367	0.1624	0.1675	0.1799	0.1881	0.2055	0.2342
18.	115.	0.80	98.8	57.77	87.79	25.64	112.4	−0.1520	−0.1365	−0.0449	0.0672	0.1347	0.1594	0.1635	0.1755	0.1843	0.2022	0.2309
20.	141.	0.91	12.5	15.16	25.81	8.71	210.0	−0.1151	−0.1147	−0.0650	0.0256	0.1031	0.1506	0.1726	0.1902	0.2052	0.2241	0.2512
18.	127.	0.91	30.1	15.20	25.88	8.74	114.5	−0.1468	−0.1428	−0.0904	0.0012	0.0828	0.1309	0.1544	0.1742	0.1881	0.2048	0.2315
18.	126.	0.91	80.2	40.46	68.83	23.21	114.4	−0.1295	−0.1236	−0.0701	0.0233	0.1066	0.1549	0.1792	0.2025	0.2159	0.2337	0.2597
18.	125.	0.90	90.1	45.79	77.31	25.87	114.4	−0.1230	−0.1170	−0.0616	0.0348	0.1174	0.1647	0.1868	0.2069	0.2203	0.2379	0.2639
18.	124.	0.90	100.5	51.02	86.28	28.92	114.4	−0.1225	−0.1168	−0.0619	0.0338	0.1159	0.1639	0.1862	0.2086	0.2225	0.2407	0.2658

Table X. Concluded

Run	Point	CP12	CP13	CP14	CP15	CP16	CP17	CP18	CP19	CP20	CP21
21.	147.	0.3272	0.2842	−0.1515	−0.1389	0.1775	0.6579	0.3573	−0.0524	−0.0859	−0.6533
19.	136.	0.3383	0.3138	−0.1486	−0.1482	0.1864	0.7089	0.3706	−0.0569	−0.0895	−0.6954
18.	111.	0.3376	0.4079	−0.1562	−0.1504	0.1962	0.7457	0.3817	−0.0567	−0.0895	−0.7047
18.	110.	0.3473	0.4518	−0.1628	−0.1554	0.2024	0.7697	0.4037	−0.0573	−0.0918	−0.7374
18.	109.	0.3451	0.4548	−0.1624	−0.1540	0.2017	0.7764	0.4035	−0.0561	−0.0904	−0.7352
21.	146.	0.3407	0.3021	−0.1359	−0.1250	0.1964	0.6748	0.3695	−0.0450	−0.0784	−0.6704
20.	140.	0.3356	0.3134	−0.1415	−0.1428	0.1958	0.7173	0.3695	−0.0570	−0.0913	−0.7228
18.	112.	0.3399	0.4150	−0.1419	−0.1335	0.2080	0.7640	0.3842	−0.0448	−0.0802	−0.7228
18.	113.	0.3499	0.4604	−0.1413	−0.1400	0.2202	0.7916	0.4036	−0.0482	−0.0855	−0.7367
18.	114.	0.3494	0.4606	−0.1506	−0.1407	0.2135	0.7894	0.4026	−0.0523	−0.0878	−0.7460
18.	115.	0.3484	0.4611	−0.1579	−0.1474	0.2089	0.7873	0.4010	−0.0570	−0.0929	−0.7528
20.	141.	0.3507	0.3364	−0.1156	−0.1138	0.2103	0.7055	0.3812	−0.0392	−0.0694	−0.6823
18.	127.	0.3333	0.3857	−0.1421	−0.1429	0.1967	0.7220	0.3678	−0.0649	−0.0972	−0.7390
18.	126.	0.3630	0.4505	−0.1255	−0.1258	0.2228	0.7611	0.4028	−0.0463	−0.0803	−0.7268
18.	125.	0.3681	0.4572	−0.1262	−0.1192	0.2230	0.7614	0.4077	−0.0423	−0.0747	−0.7174
18.	124.	0.3678	0.4627	−0.1241	−0.1187	0.2260	0.7629	0.4073	−0.0425	−0.0745	−0.7164

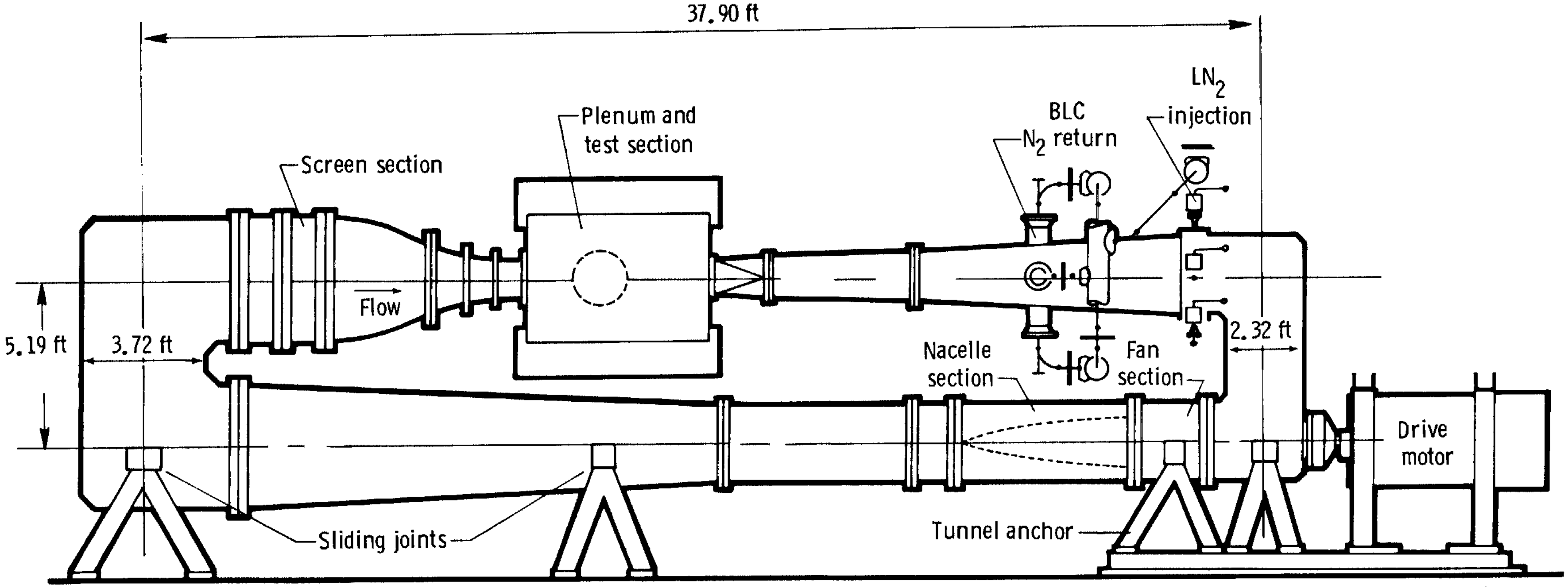

Figure 1. Langley 0.3-m TCT with 13-in. by 13-in. two-dimensional test section installed.

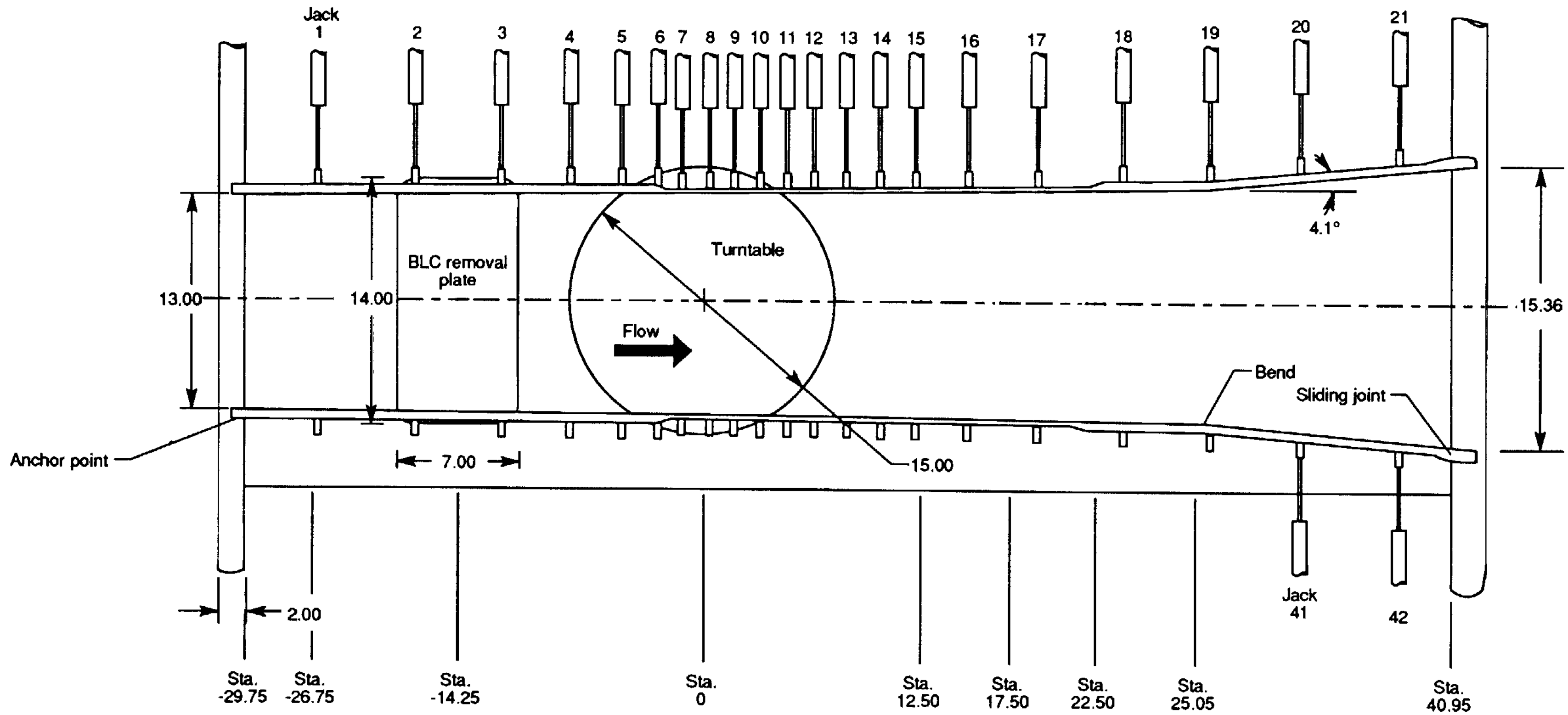

Figure 2. Details of flow region of 13-in. by 13-in. adaptive wall test section. All dimensions are in inches; some lower wall jacks omitted for clarity.

ORIGINAL PAGE
BLACK AND WHITE PHOTOGRAPH

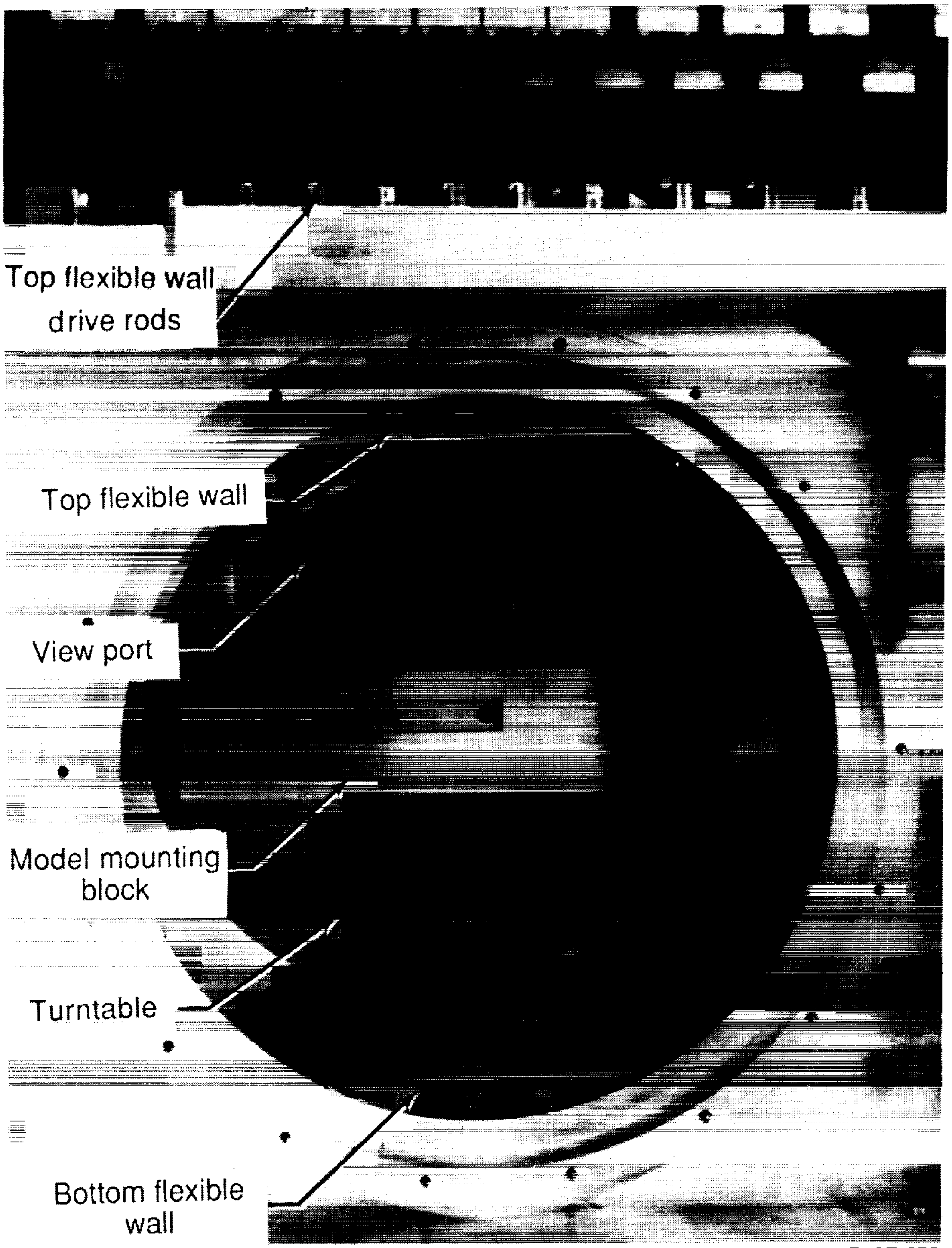

Figure 3. Model mounting system of 13-in. by 13-in. adaptive wall test section.

L-90-11841

Figure 4. High Reynolds number cavity model prior to tunnel installation.

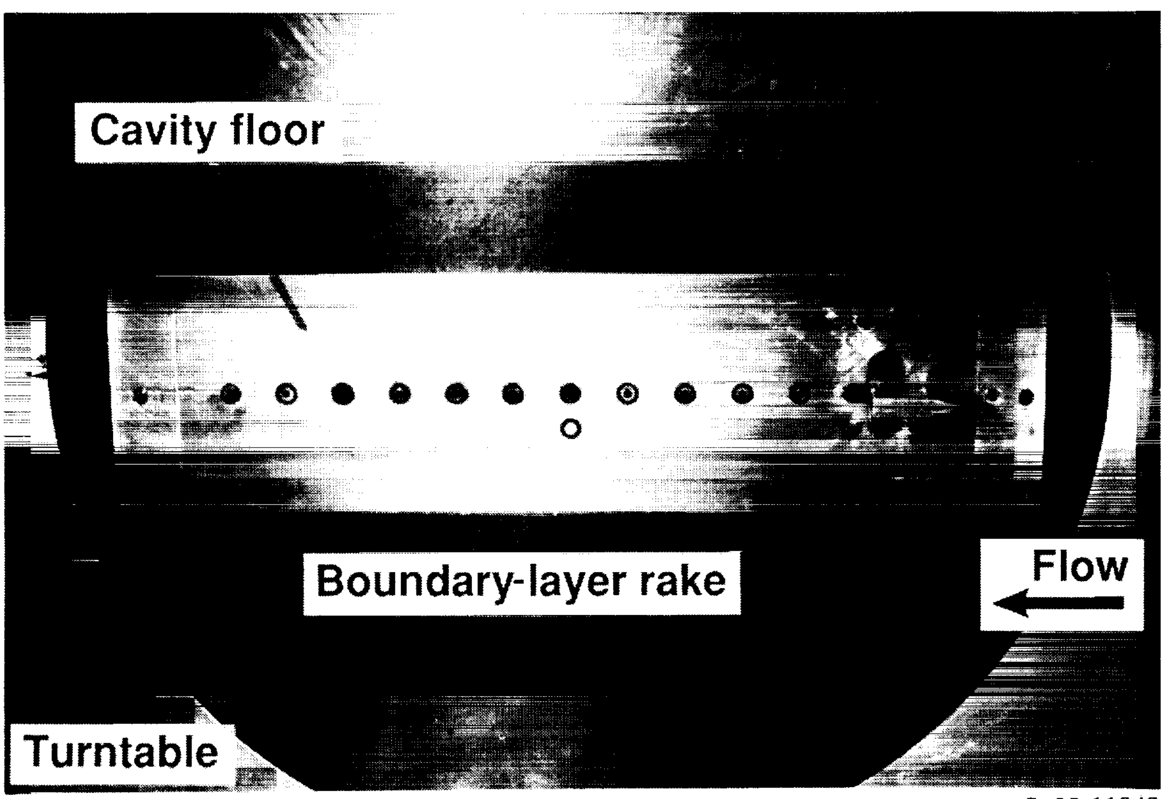

L-90-11842

Figure 5. Model installed in tunnel.

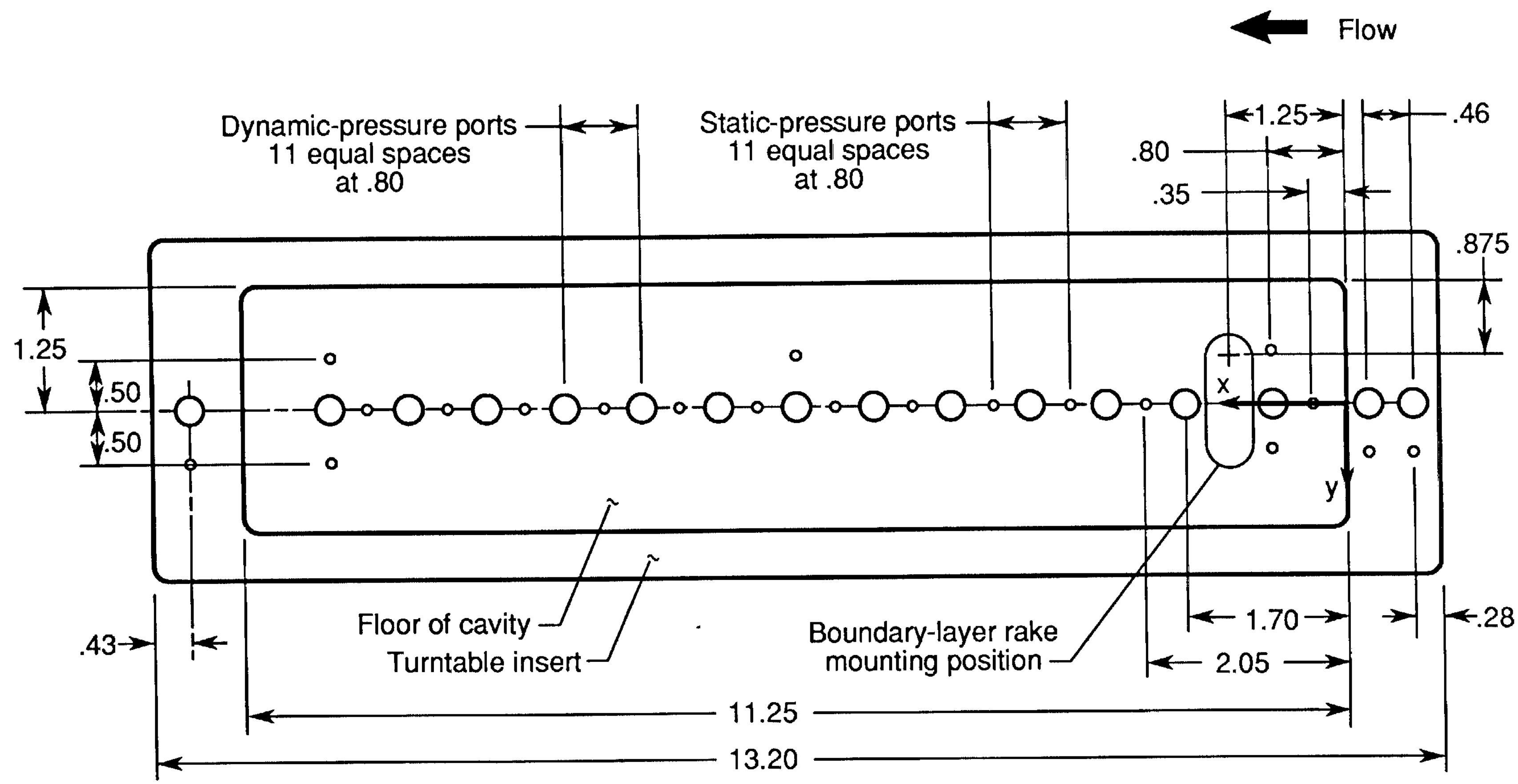

Figure 6. Instrumentation layout. All dimensions are in inches.

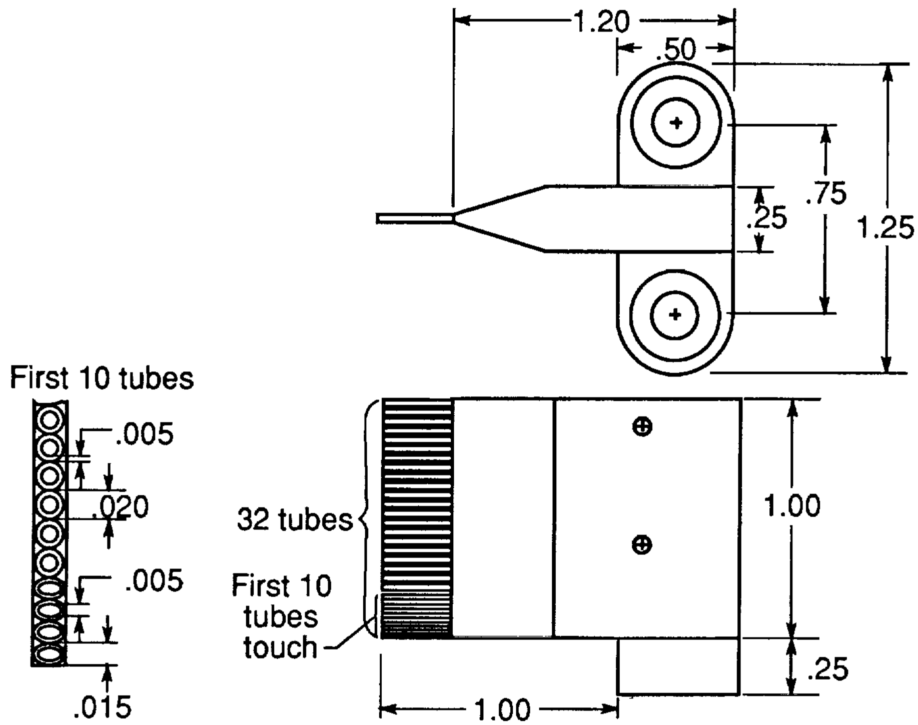

Figure 7. Boundary-layer rake. All dimensions are in inches.

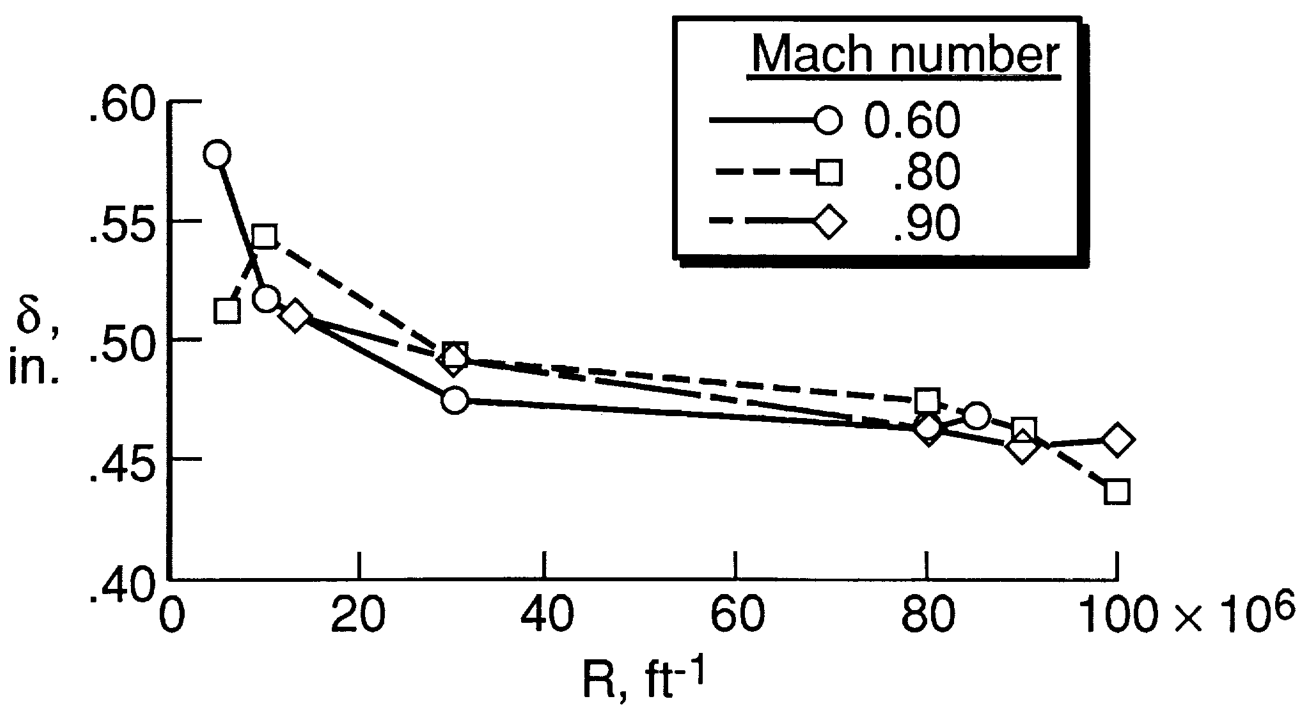

Figure 8. Variation in boundary-layer thickness with Reynolds number.

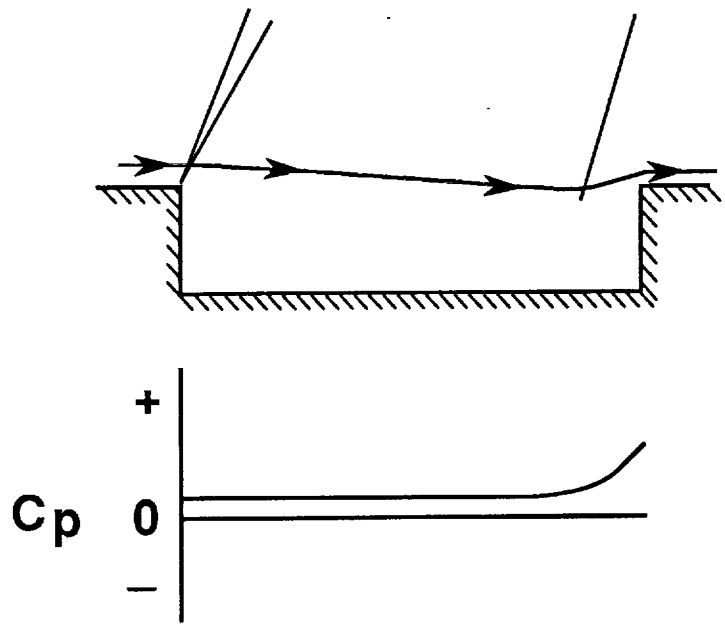

(a) Open cavity flow; $l/h < 10$.

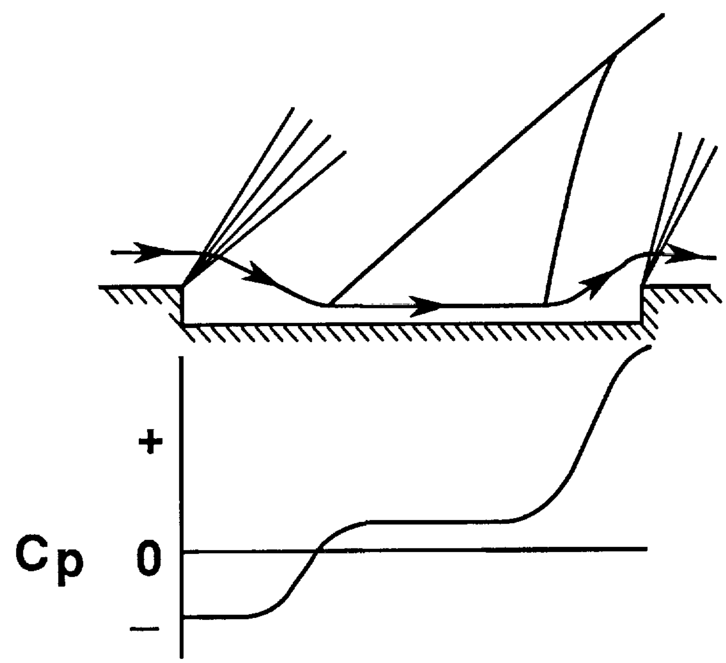

(b) Closed cavity flow; $l/h > 13$.

Figure 9. Flow-field sketches and typical mean pressure distributions for cavity flow types at subsonic speeds.

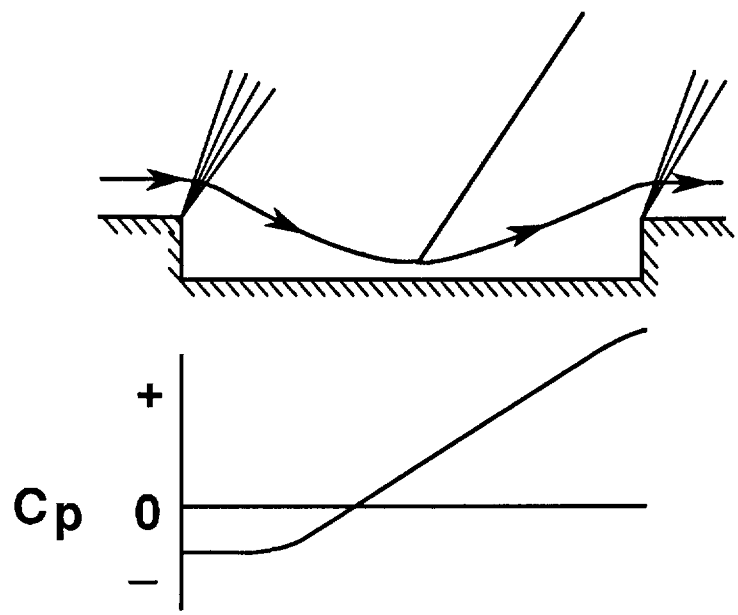

(c) Transitional-closed cavity flow; $10 < l/h < 13$.

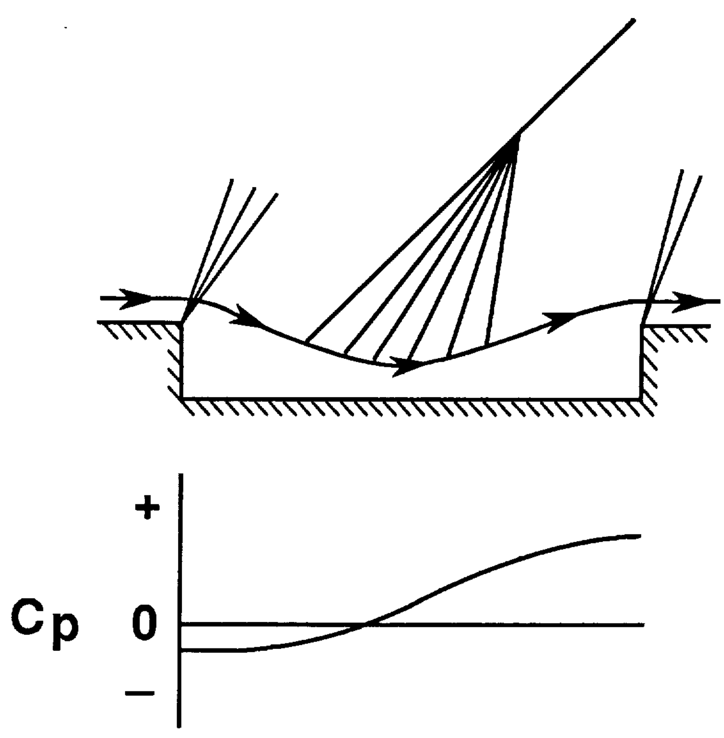

(d) Transitional-open cavity flow; $10 < l/h < 13$.

Figure 9. Concluded.

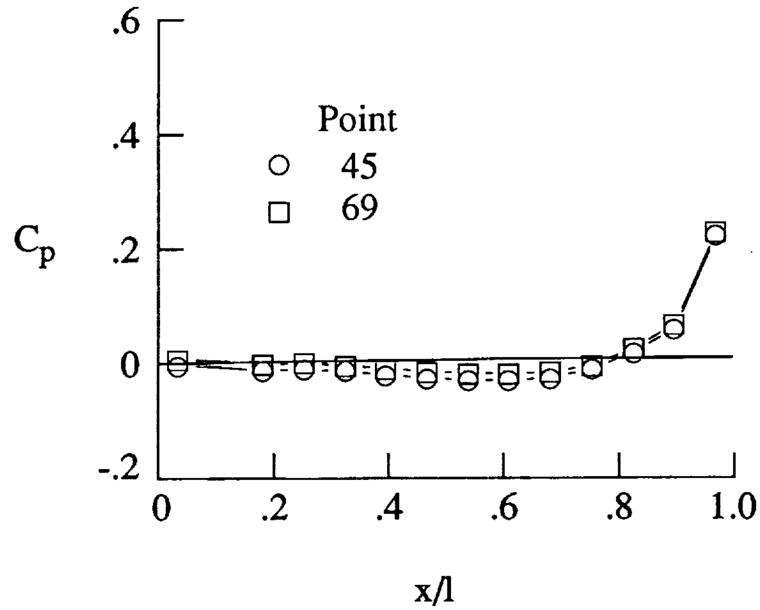

(a) Repeat points at constant free-stream conditions; $p_{t,\infty} = 29$ psi; $T_{t,\infty} = 105°$F.

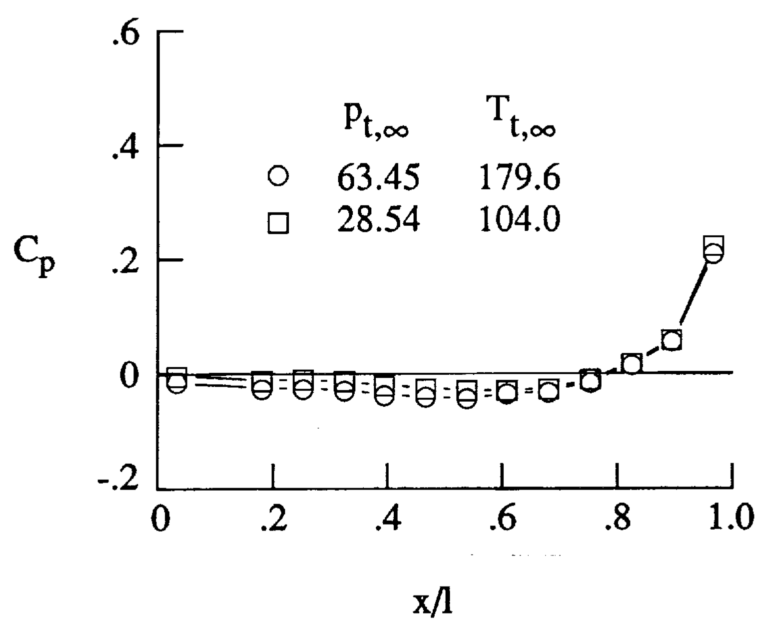

(b) Repeat points at different free-stream conditions.

Figure 10. Repeatability of mean pressure data at $M_\infty = 0.60$ and $R = 30 \times 10^6$ ft^{-1} for $l/h = 4.4$.

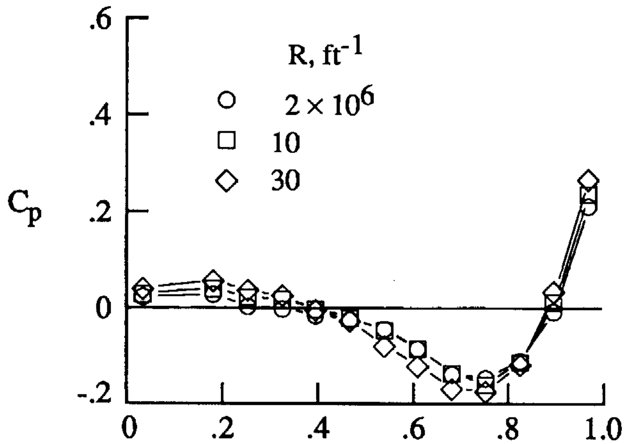

(a) $M_\infty = 0.20$.

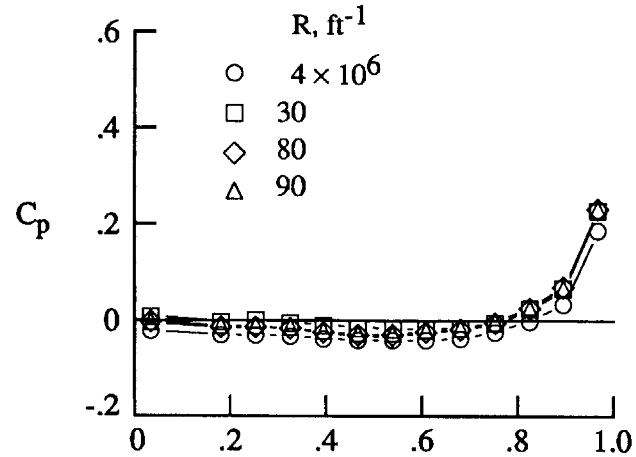

(b) $M_\infty = 0.60$.

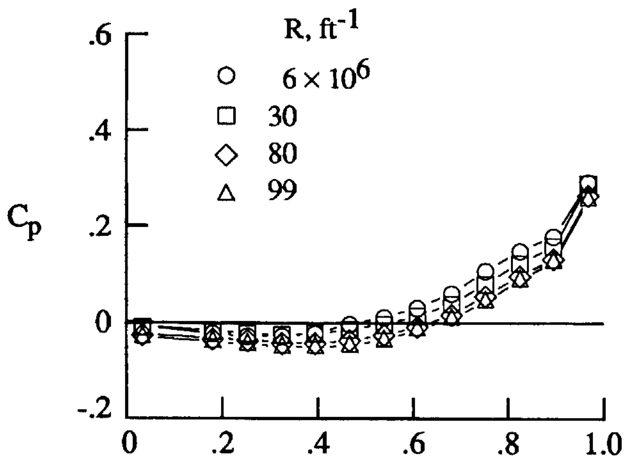

(c) $M_\infty = 0.80$.

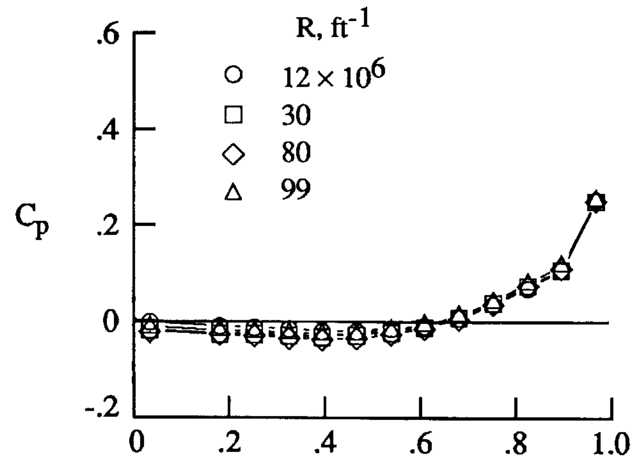

(d) $M_\infty = 0.90$.

Figure 11. Effect of Reynolds number on cavity pressure distributions for $l/h = 4.4$. $0.17 \leq \delta/h \leq 0.23$; $\psi = 0°$.

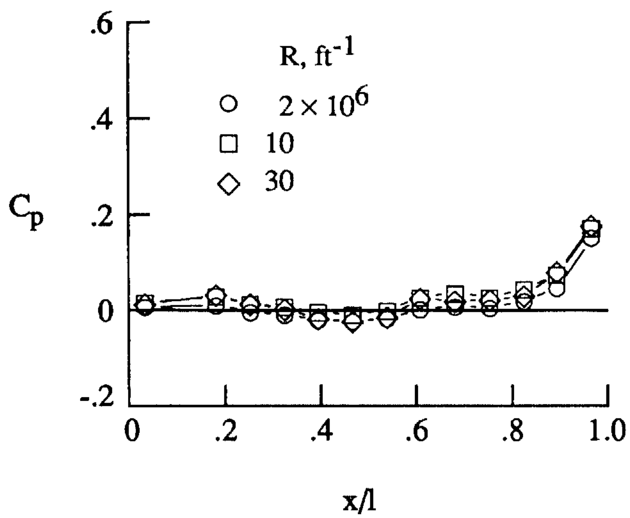

(a) $M_\infty = 0.20$.

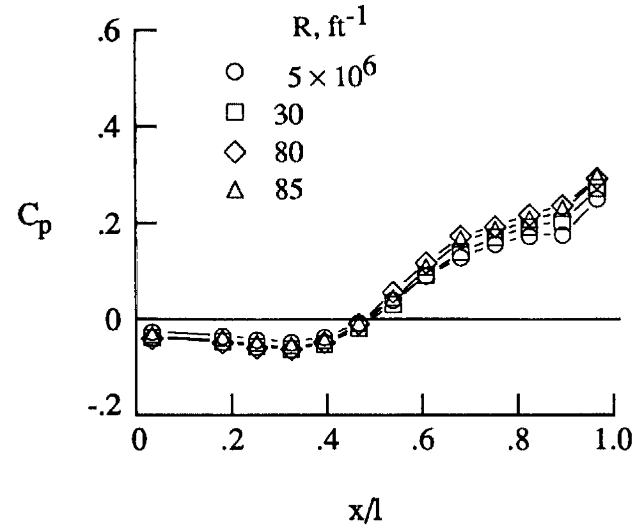

(b) $M_\infty = 0.60$.

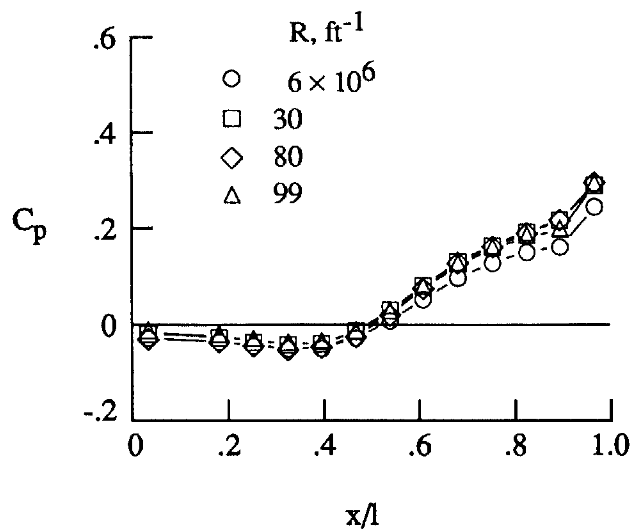

(c) $M_\infty = 0.80$.

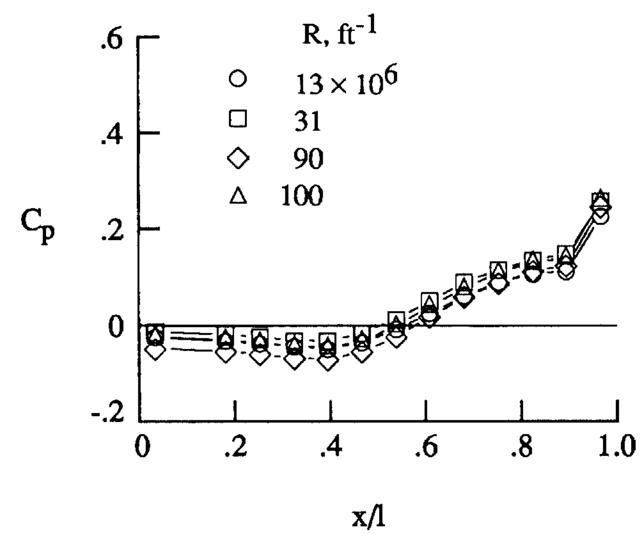

(d) $M_\infty = 0.90$.

Figure 12. Effect of Reynolds number on cavity pressure distributions for $l/h = 6.7$. $0.26 \leq \delta/h \leq 0.34$; $\psi = 0°$.

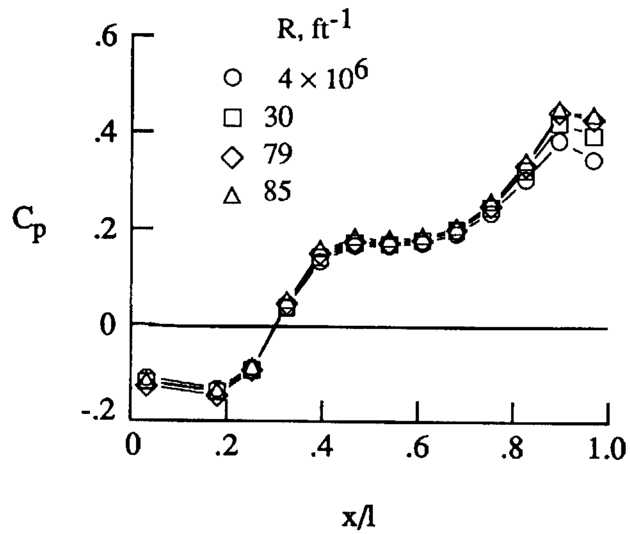

(a) $M_\infty = 0.60$.

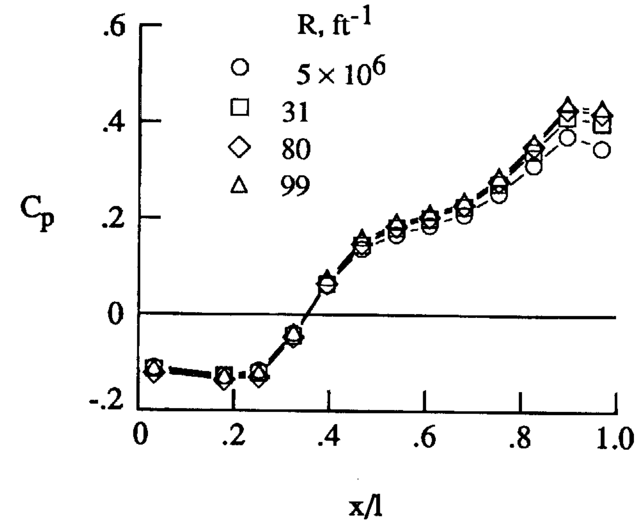

(b) $M_\infty = 0.80$.

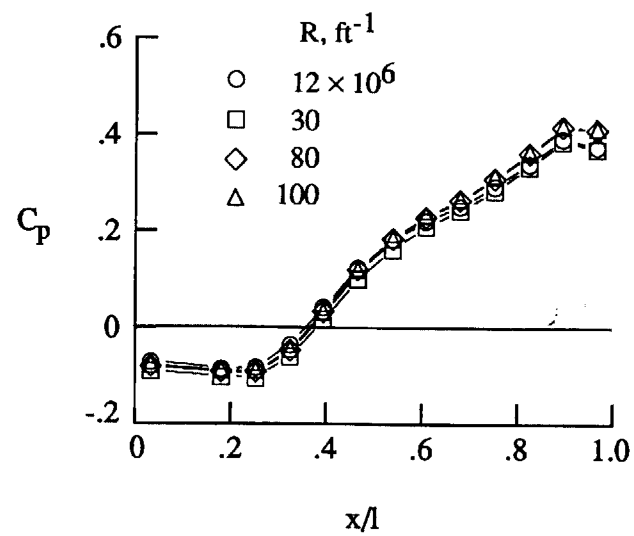

(c) $M_\infty = 0.90$.

Figure 13. Effect of Reynolds number on cavity pressure distributions for $l/h = 12.67$. $0.49 \leq \delta/h \leq 0.65$; $\psi = 0°$.

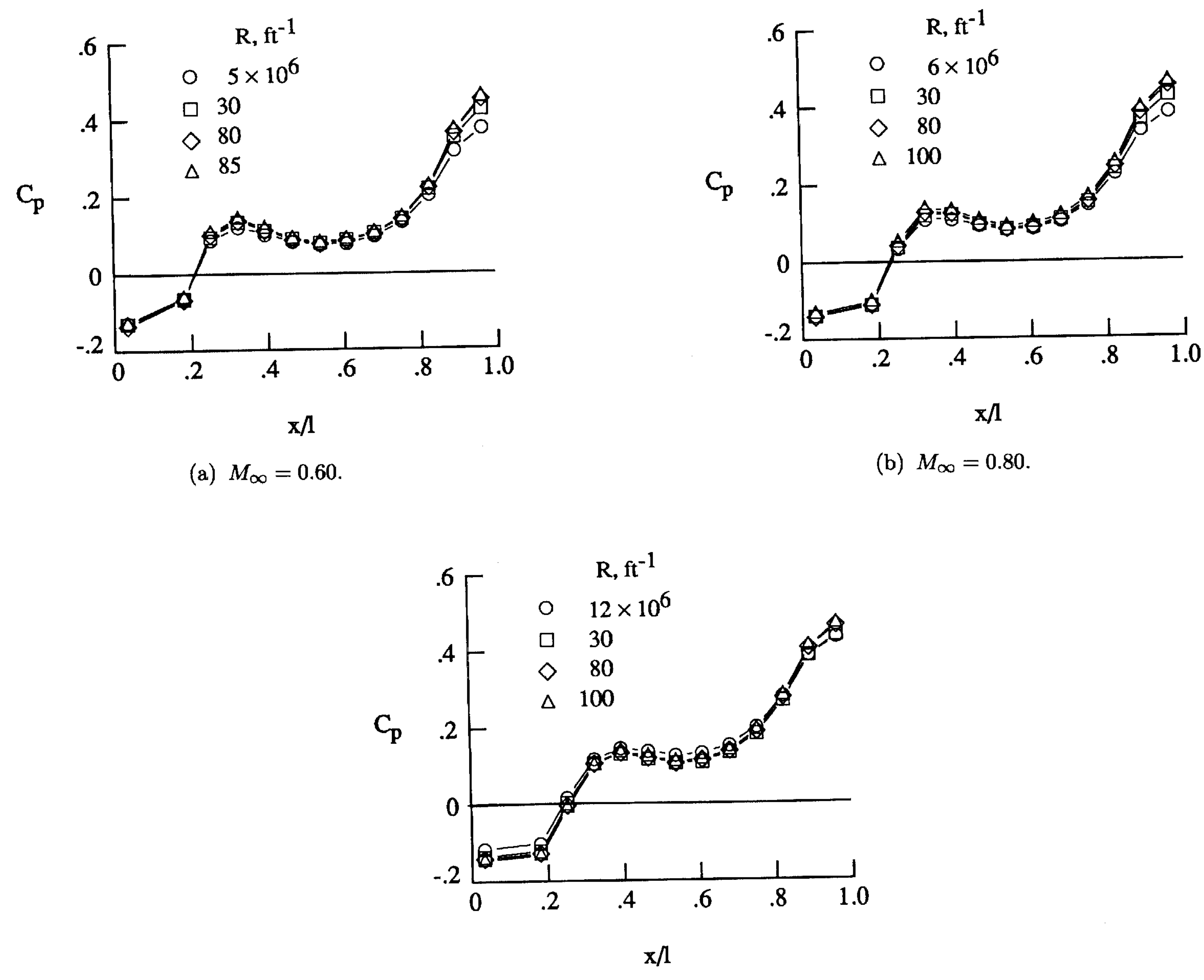

(a) $M_\infty = 0.60$.

(b) $M_\infty = 0.80$.

(c) $M_\infty = 0.90$.

Figure 14. Effect of Reynolds number on cavity pressure distributions for $l/h = 20.0$. $0.78 \leq \delta/h \leq 1.03$; $\psi = 0°$.

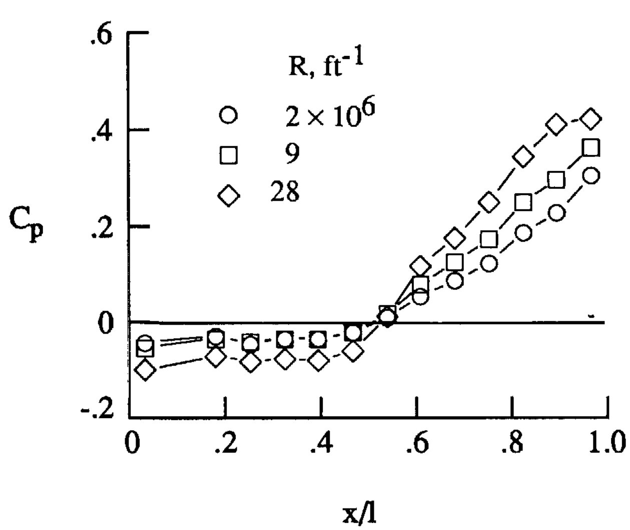

(a) $M_\infty = 0.20$.

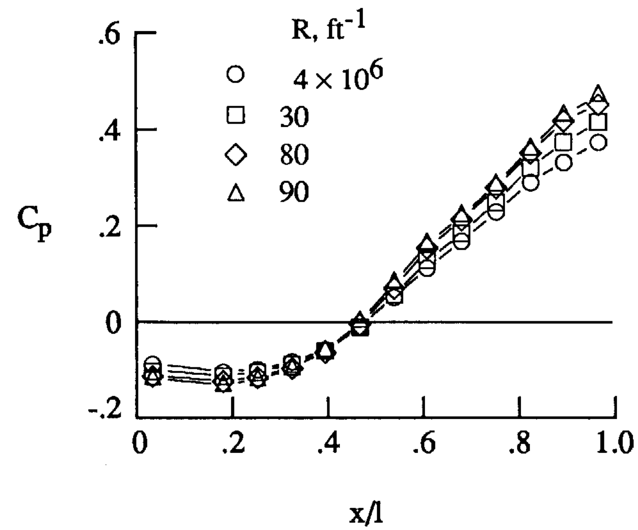

(b) $M_\infty = 0.60$.

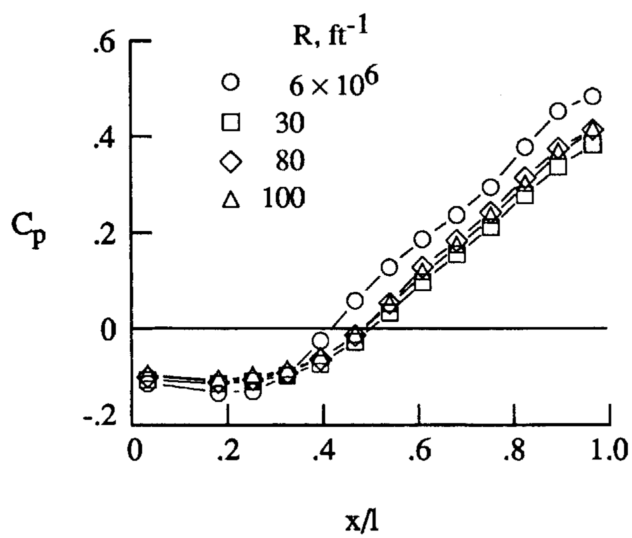

(c) $M_\infty = 0.80$.

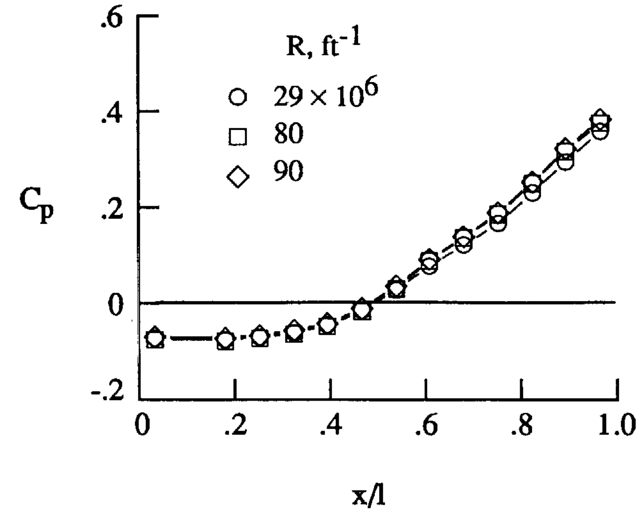

(d) $M_\infty = 0.90$.

Figure 15. Effect of Reynolds number on cavity pressure distributions for $l/h = 4.4$. $0.17 \leq \delta/h \leq 0.23$; $\psi = 15°$.

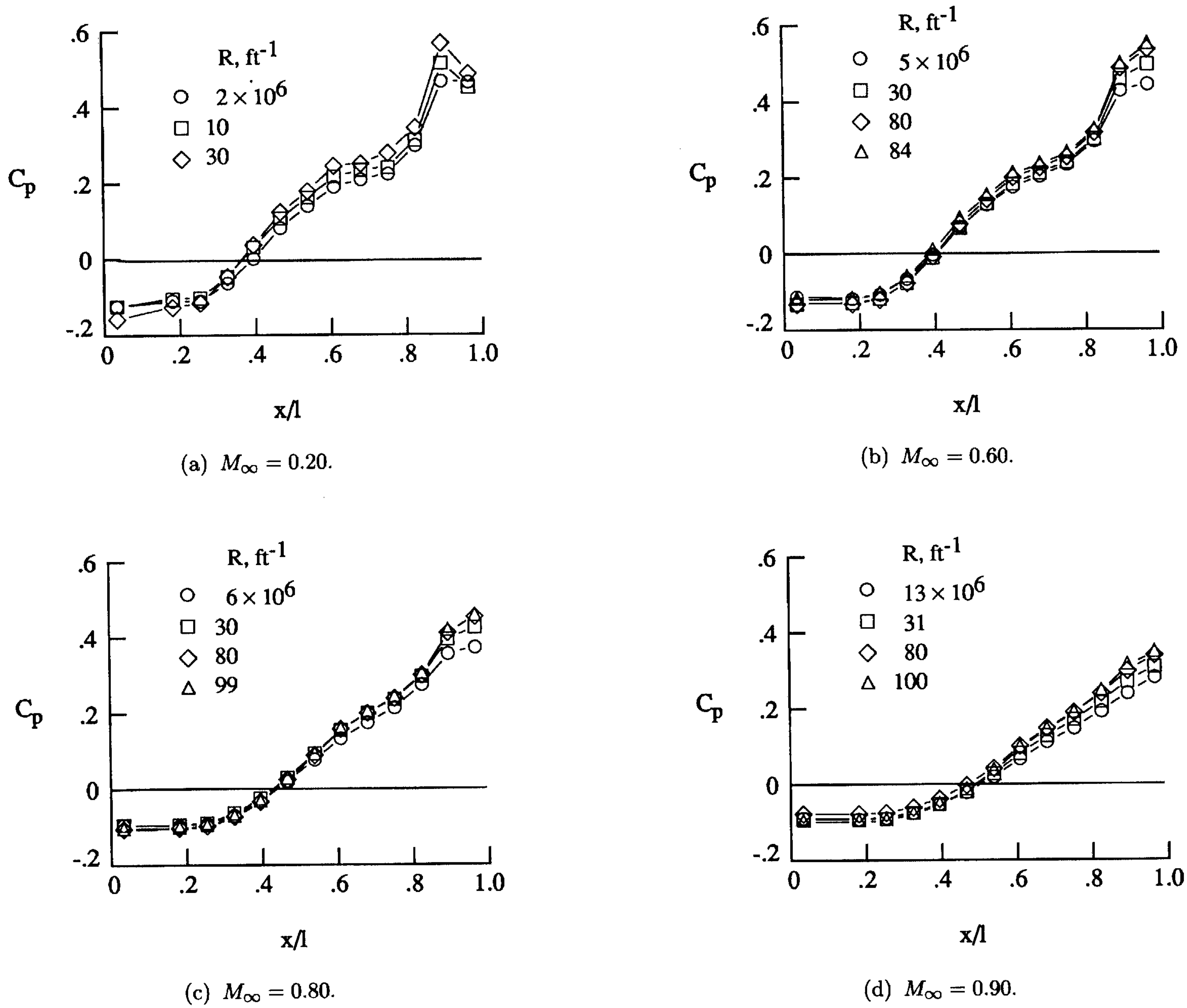

Figure 16. Effect of Reynolds number on cavity pressure distributions for $l/h = 6.7$. $0.26 \leq \delta/h \leq 0.34$; $\psi = 15°$.

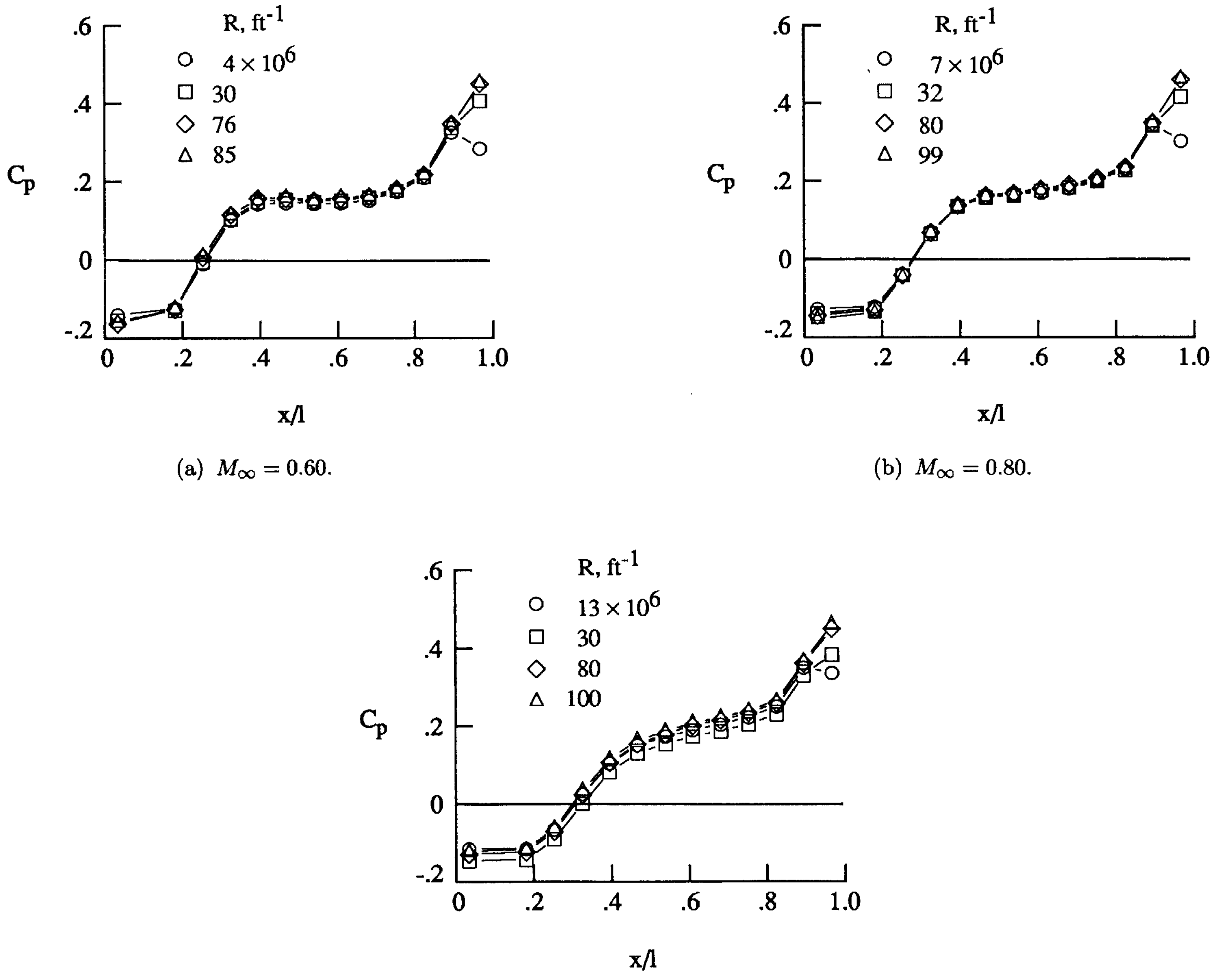

(a) $M_\infty = 0.60$.

(b) $M_\infty = 0.80$.

(c) $M_\infty = 0.90$.

Figure 17. Effect of Reynolds number on cavity pressure distributions for $l/h = 12.67$. $0.49 \leq \delta/h \leq 0.65$; $\psi = 15°$.

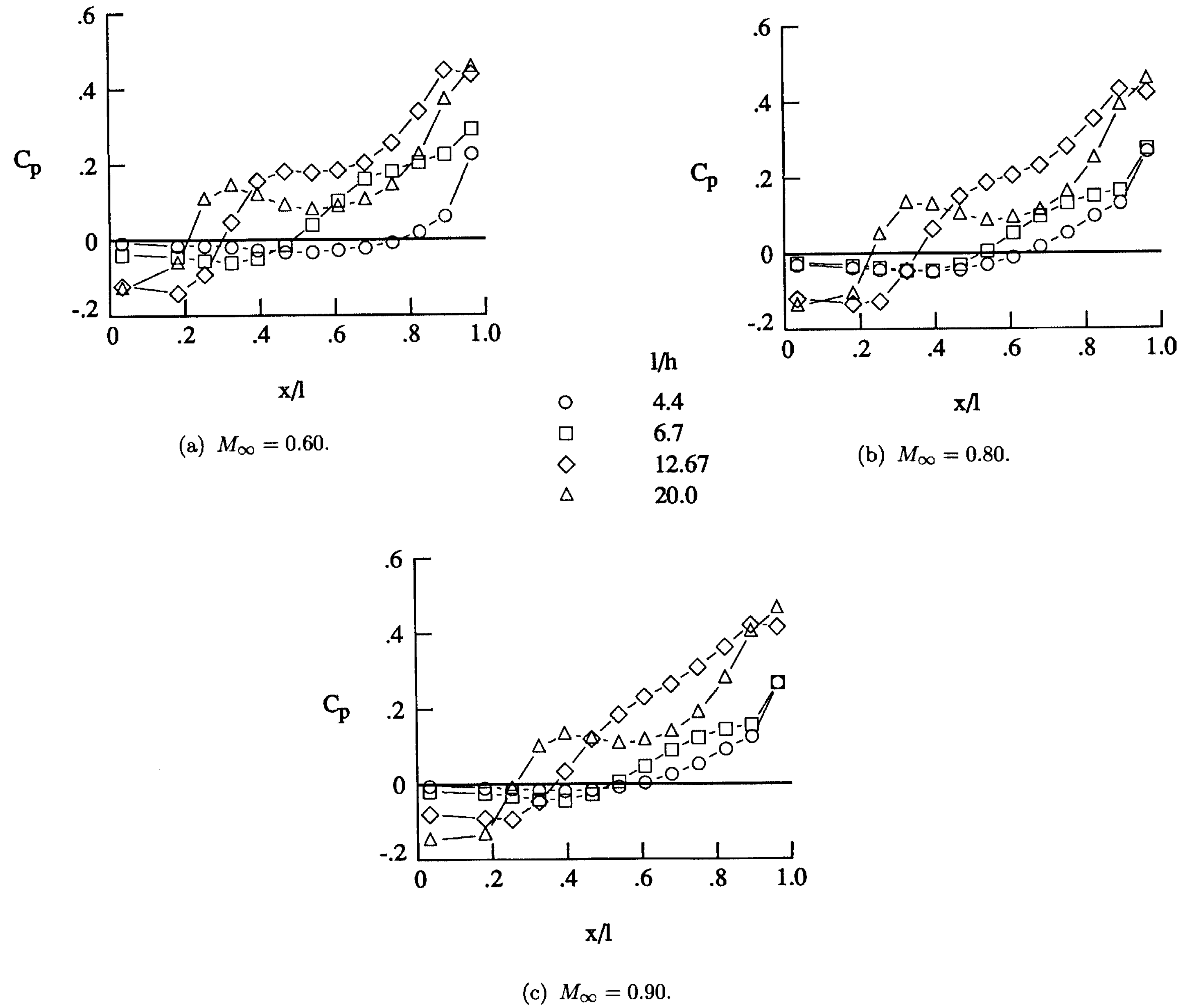

Figure 18. Effect of cavity depth on pressure distributions for $R \approx 90 \times 10^6$ and $\psi = 0°$.

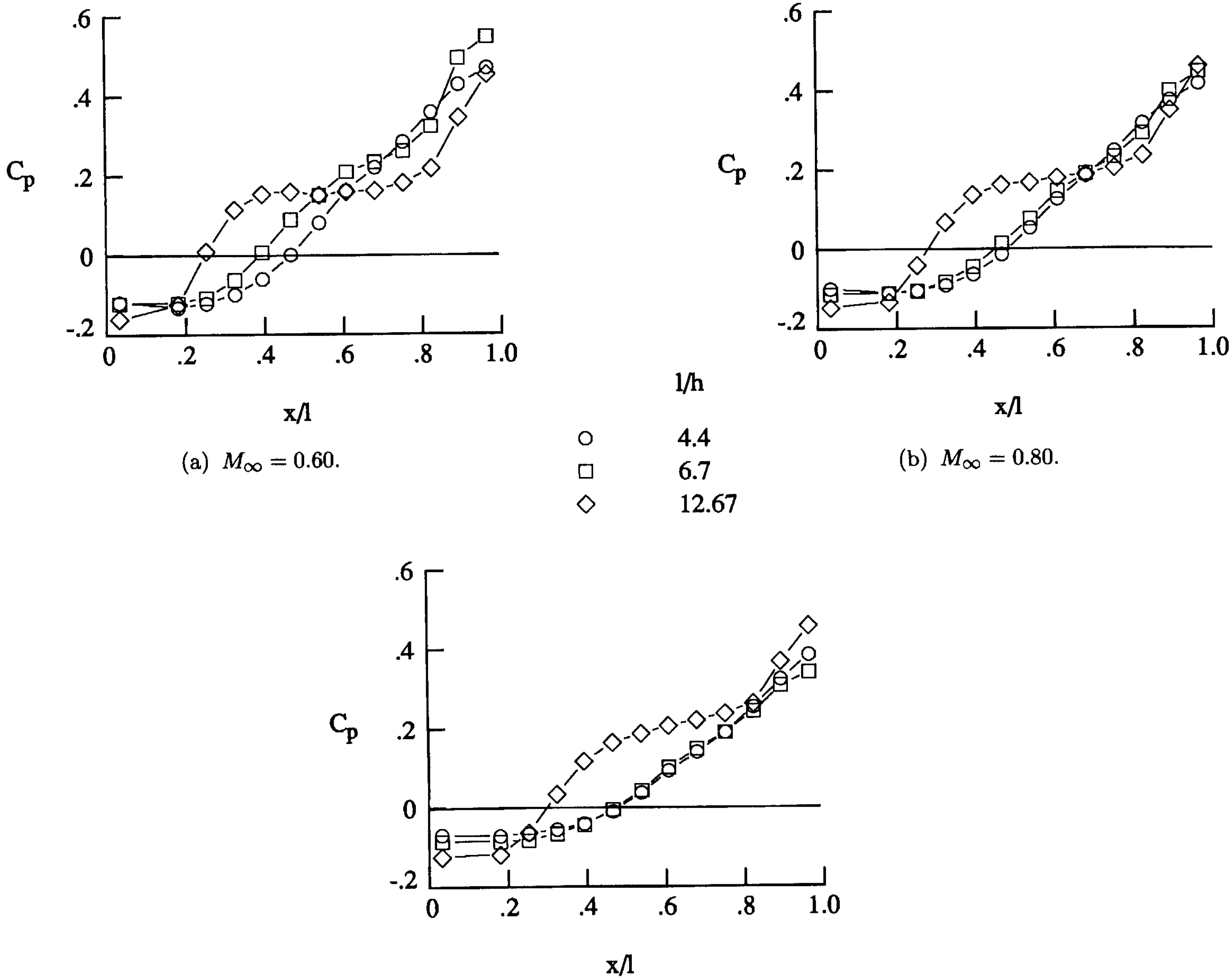

(a) $M_\infty = 0.60$.

(b) $M_\infty = 0.80$.

(c) $M_\infty = 0.90$.

Figure 19. Effect of cavity depth on pressure distributions for $R \approx 90 \times 10^6$ and $\psi = 15°$.

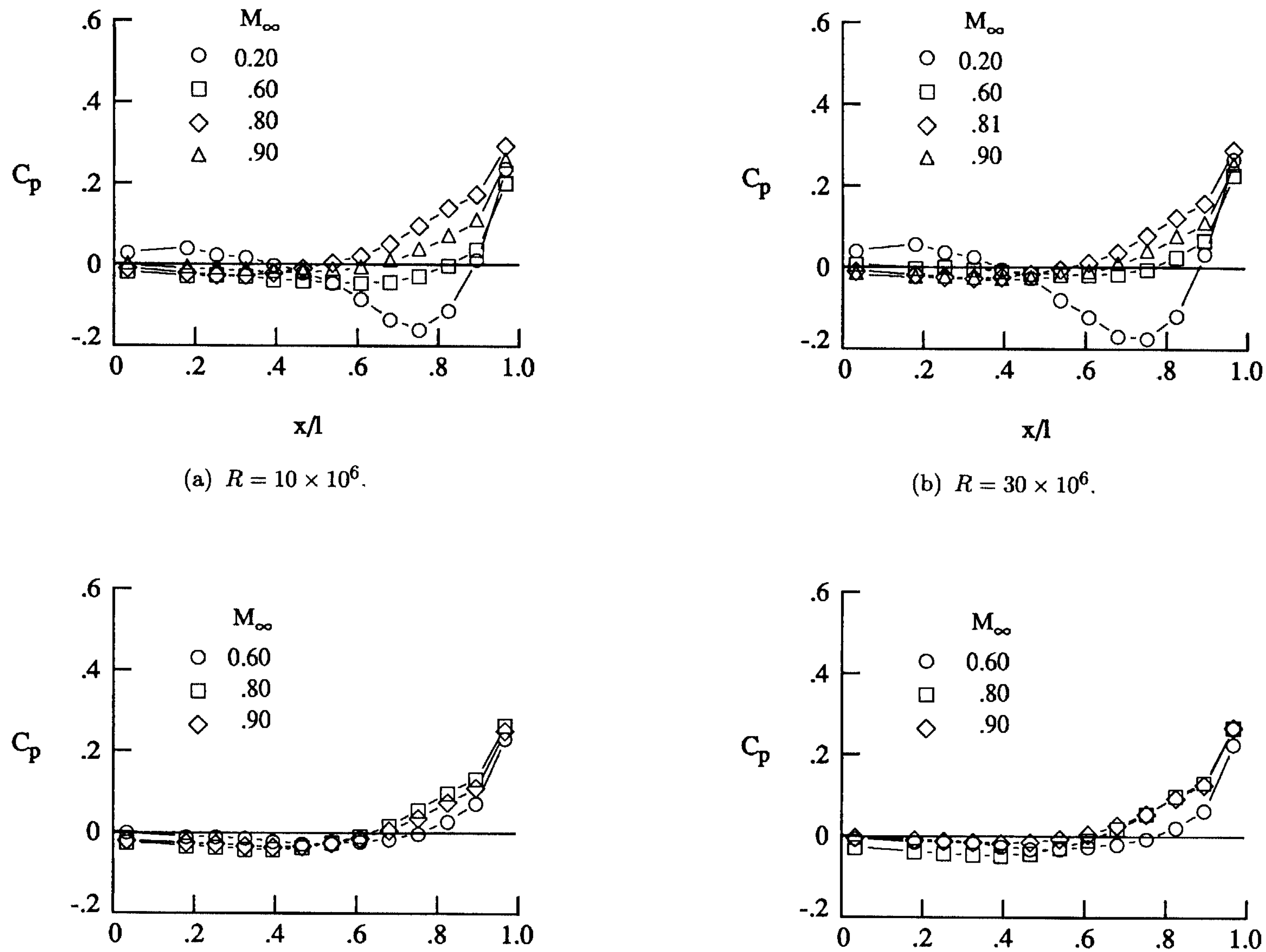

(a) $R = 10 \times 10^6$.

(b) $R = 30 \times 10^6$.

(c) $R = 80 \times 10^6$.

(d) $R = 90 \times 10^6$.

Figure 20. Effect of Mach number on cavity pressure distributions for $l/h = 4.4$ and $\psi = 0°$.

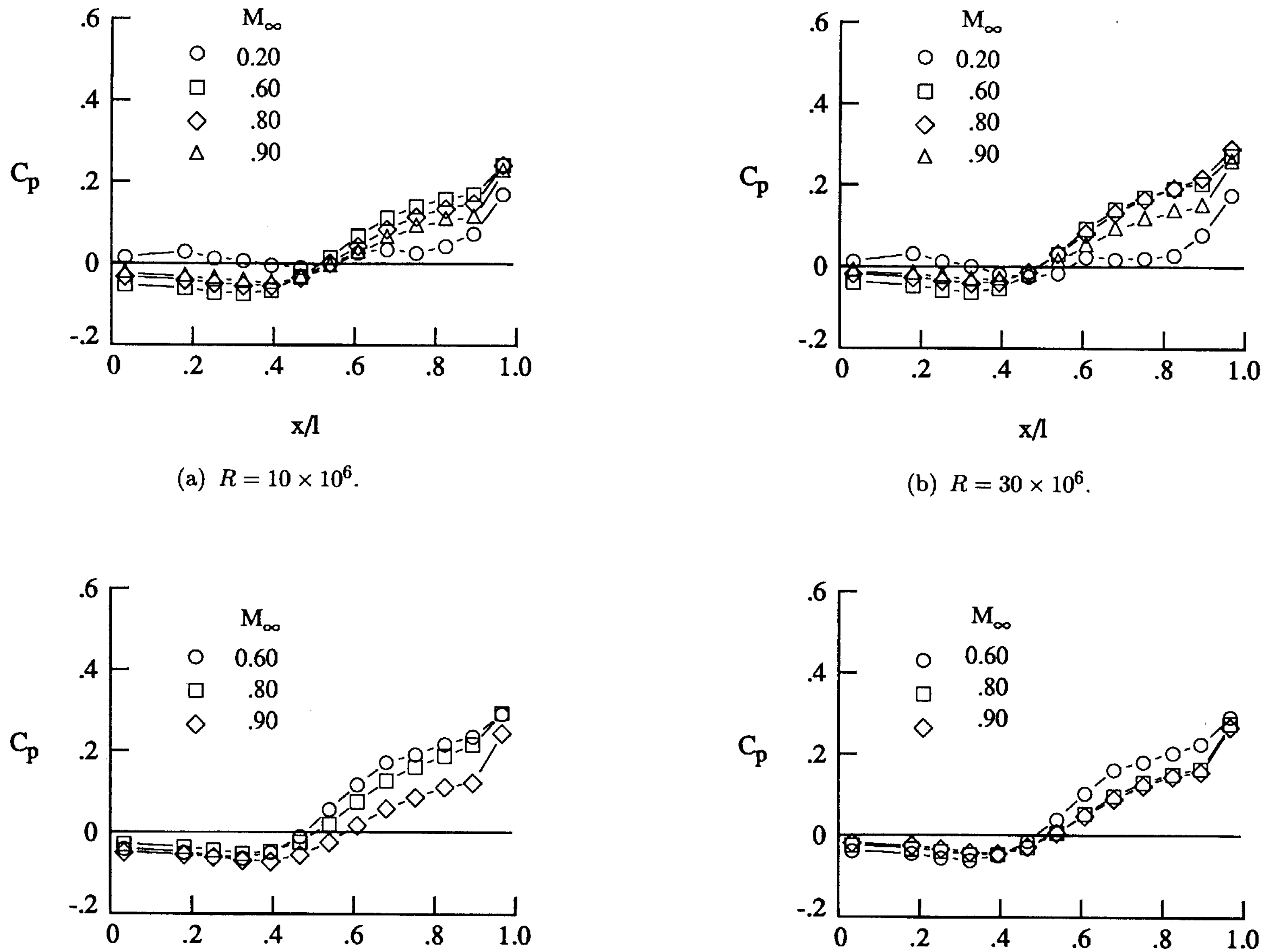

(a) $R = 10 \times 10^6$.

(b) $R = 30 \times 10^6$.

(c) $R = 80 \times 10^6$.

(d) $R = 90 \times 10^6$.

Figure 21. Effect of Mach number on cavity pressure distributions for $l/h = 6.7$ and $\psi = 0°$.

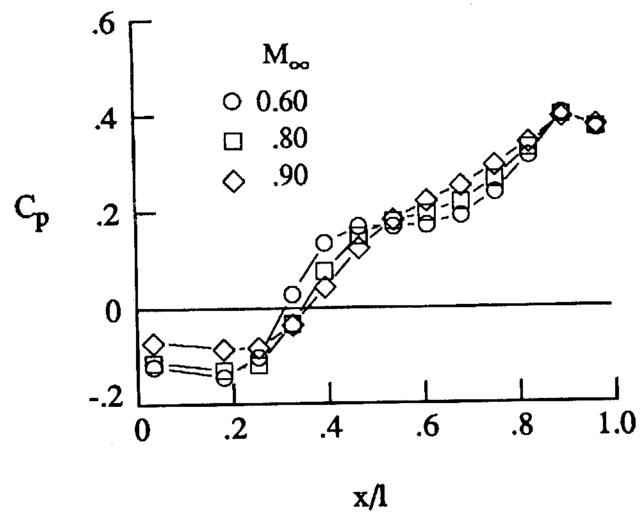

(a) $R = 10 \times 10^6$.

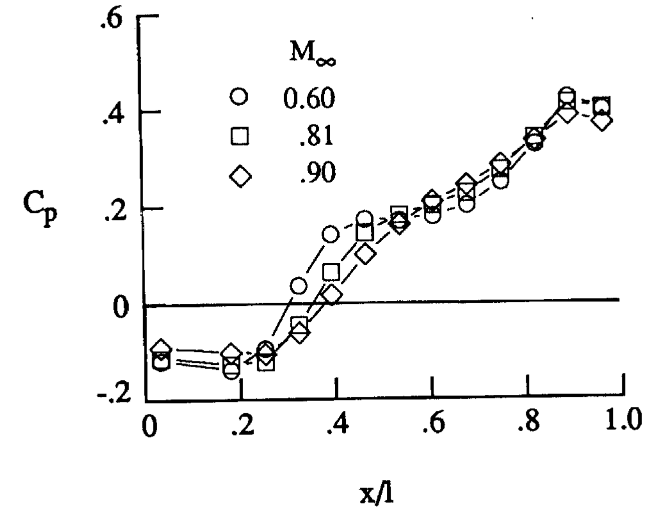

(b) $R = 30 \times 10^6$.

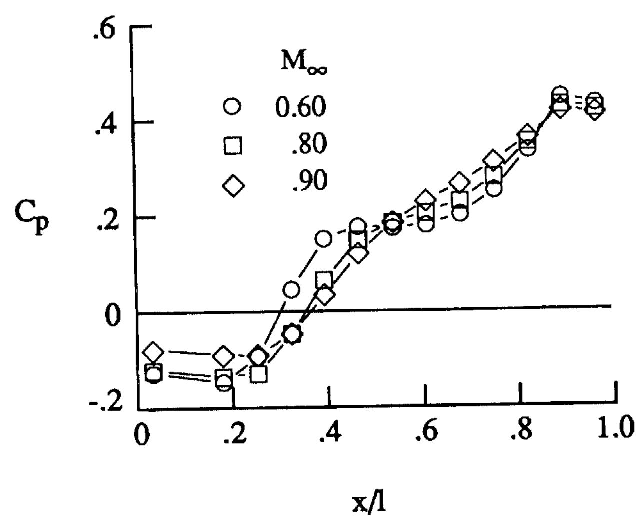

(c) $R = 80 \times 10^6$.

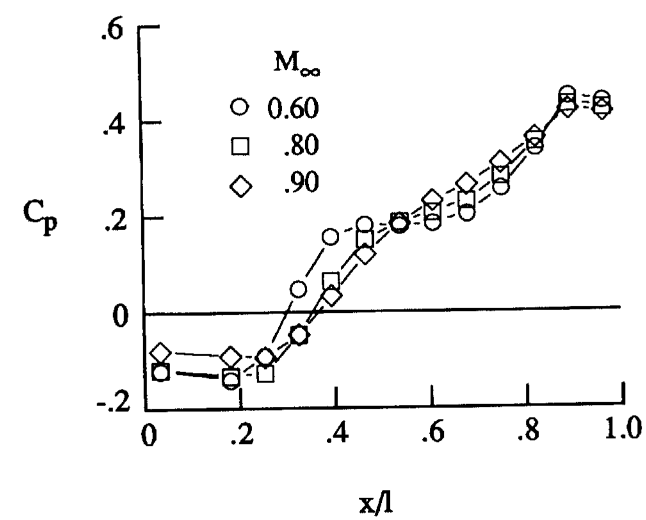

(d) $R = 90 \times 10^6$.

Figure 22. Effect of Mach number on cavity pressure distributions for $l/h = 12.67$ and $\psi = 0°$.

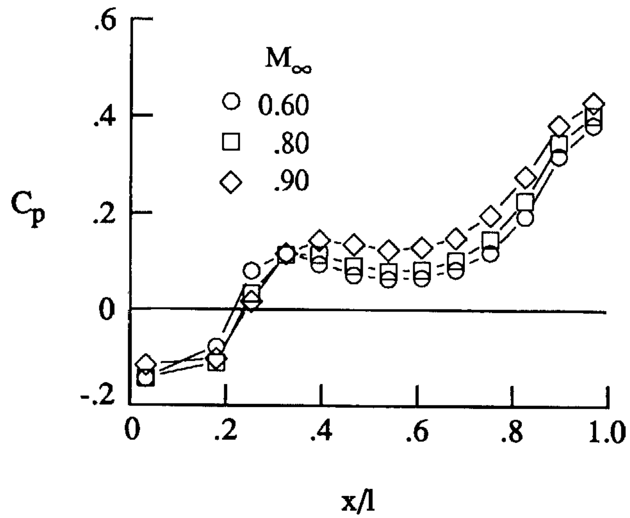

(a) $R = 10 \times 10^6$.

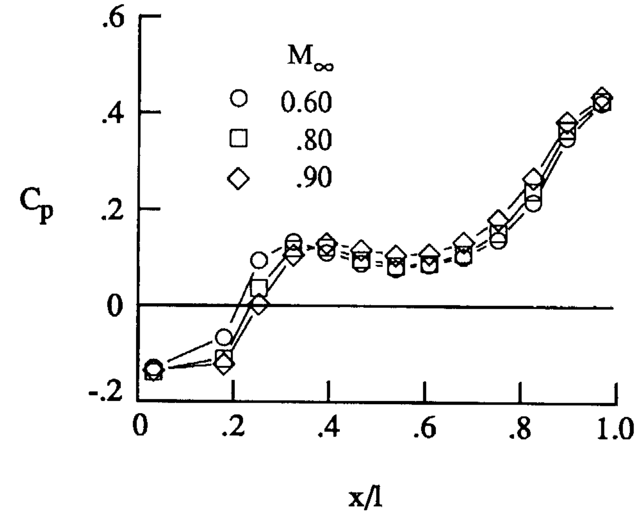

(b) $R = 30 \times 10^6$.

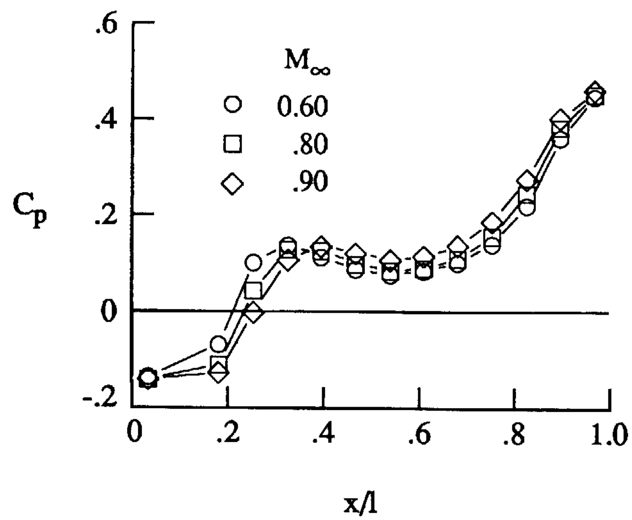

(c) $R = 80 \times 10^6$.

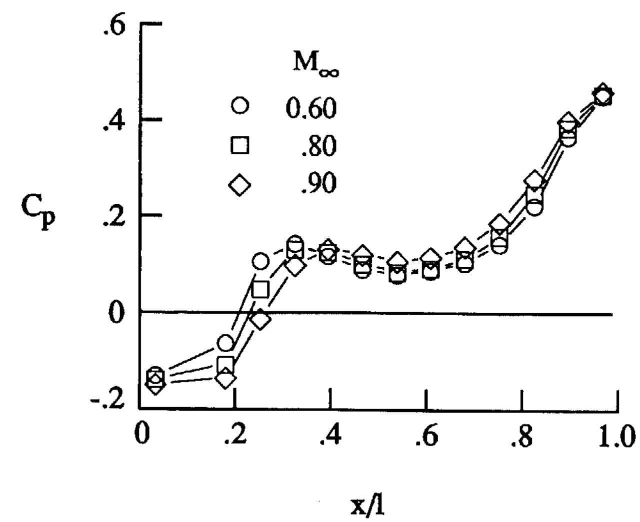

(d) $R = 90 \times 10^6$.

Figure 23. Effect of Mach number on cavity pressure distributions for $l/h = 20.0$ and $\psi = 0°$.

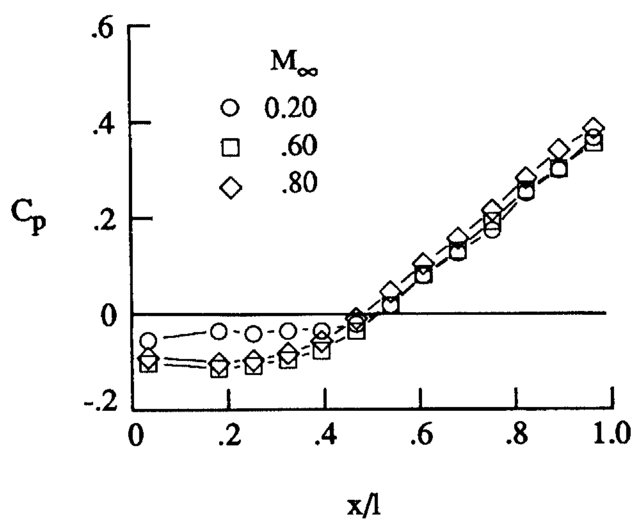

(a) $R = 10 \times 10^6$.

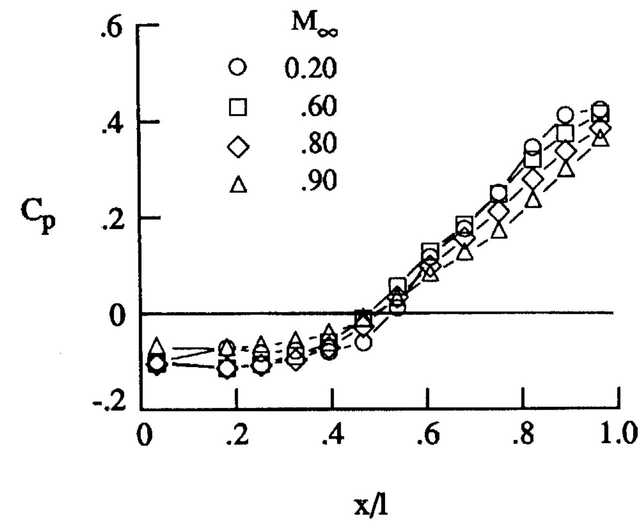

(b) $R = 30 \times 10^6$.

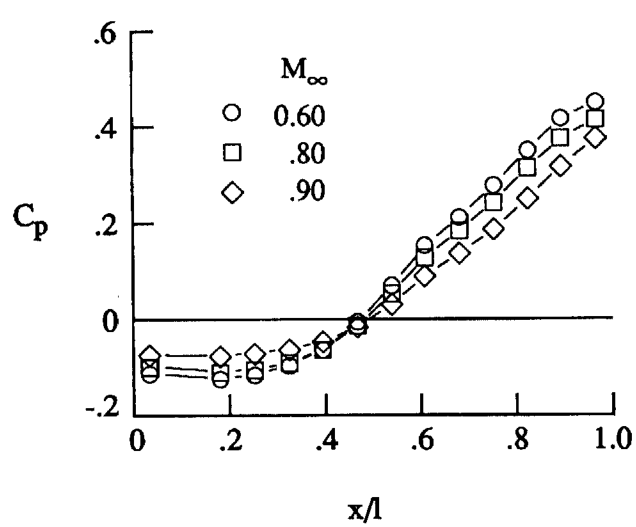

(c) $R = 80 \times 10^6$.

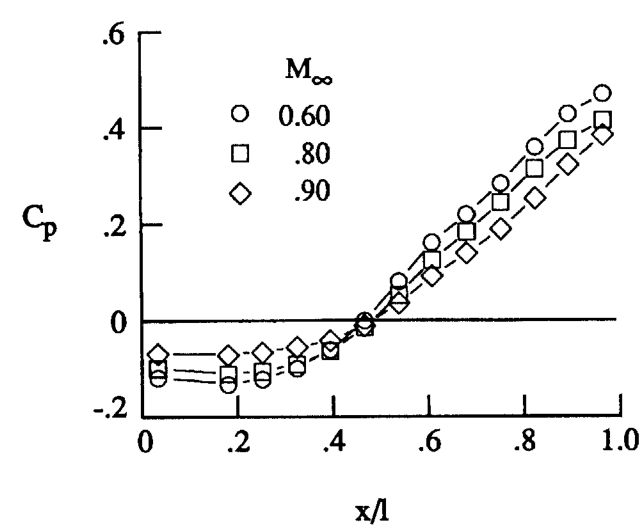

(d) $R = 90 \times 10^6$.

Figure 24. Effect of Mach number on cavity pressure distributions for $l/h = 4.4$ and $\psi = 15°$.

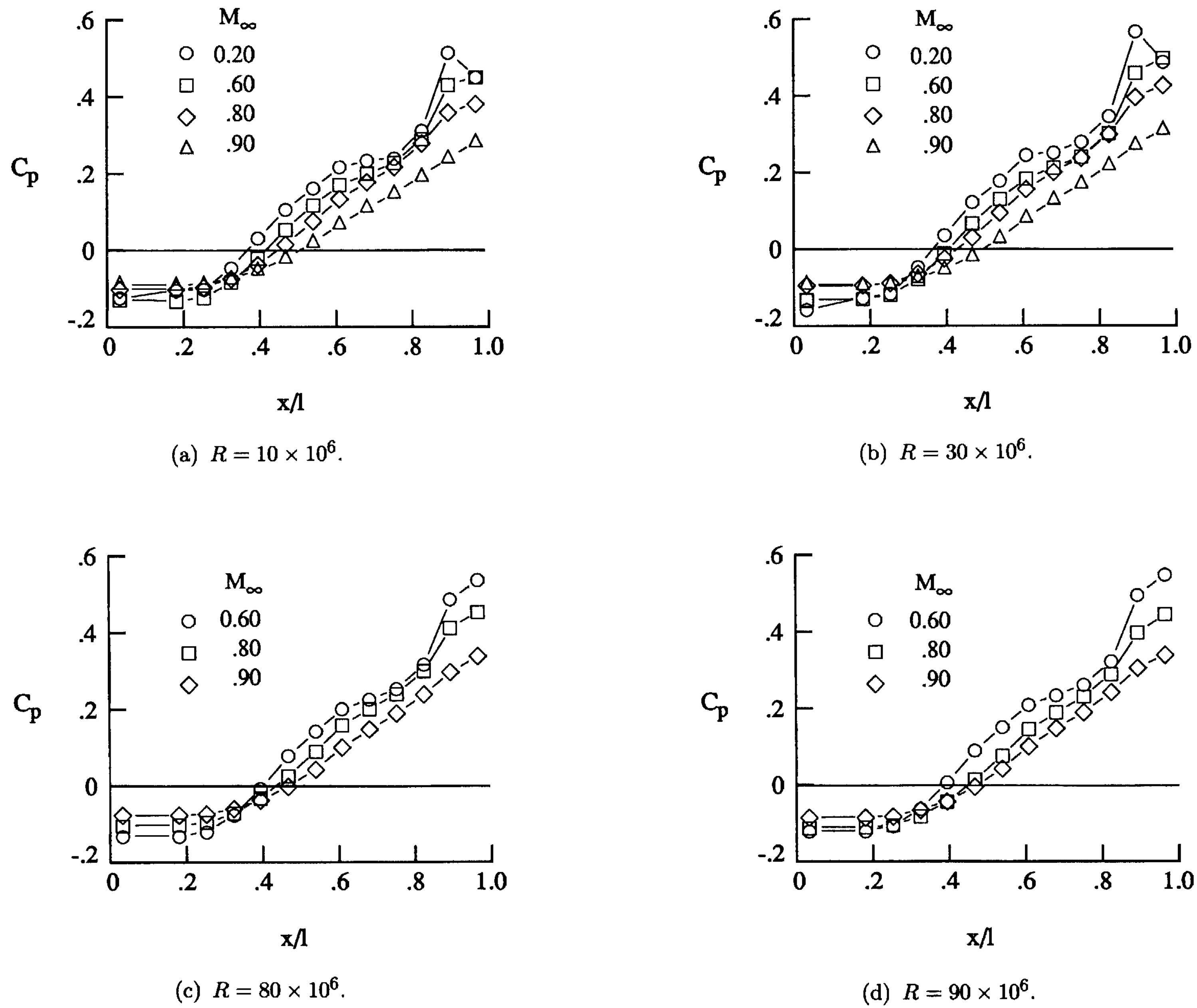

(a) $R = 10 \times 10^6$.

(b) $R = 30 \times 10^6$.

(c) $R = 80 \times 10^6$.

(d) $R = 90 \times 10^6$.

Figure 25. Effect of Mach number on cavity pressure distributions for $l/h = 6.7$ and $\psi = 15°$.

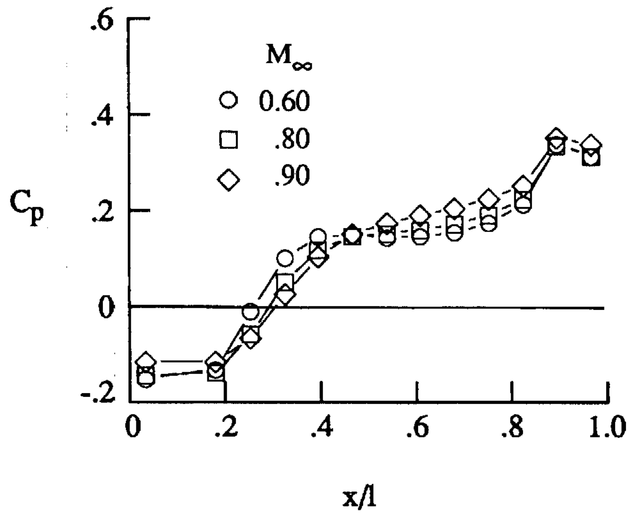

(a) $R = 10 \times 10^6$.

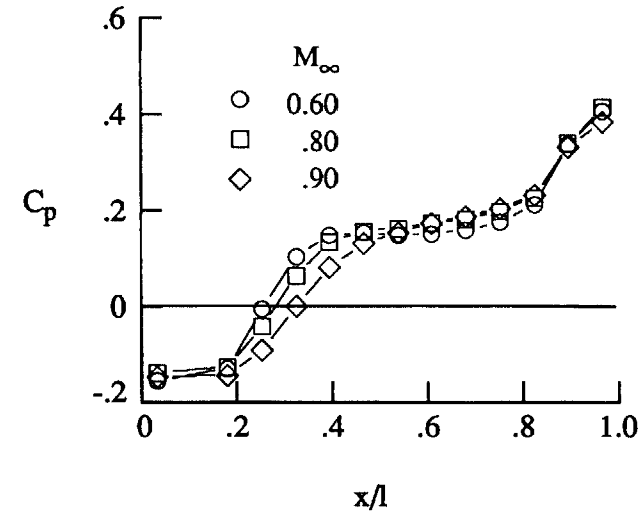

(b) $R = 30 \times 10^6$.

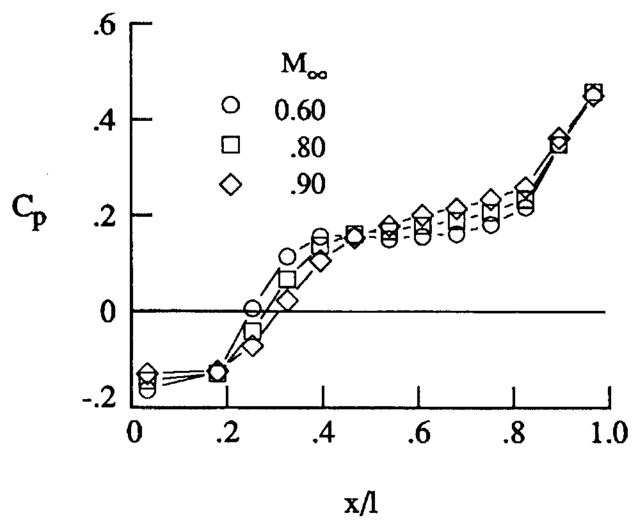

(c) $R = 80 \times 10^6$.

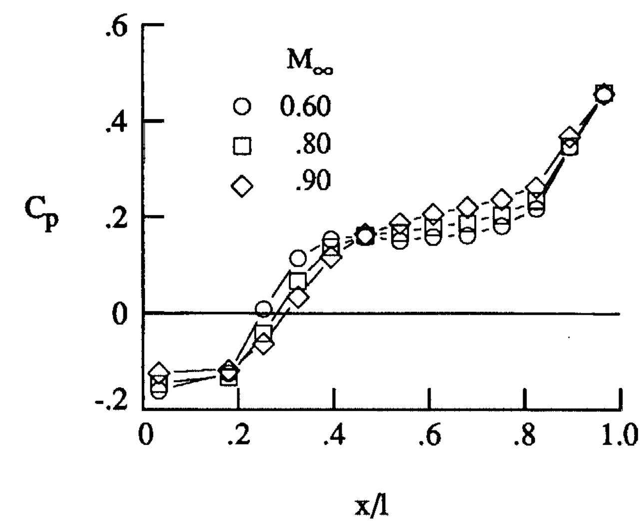

(d) $R = 90 \times 10^6$.

Figure 26. Effect of Mach number on cavity pressure distributions for $l/h = 12.67$ and $\psi = 15°$.

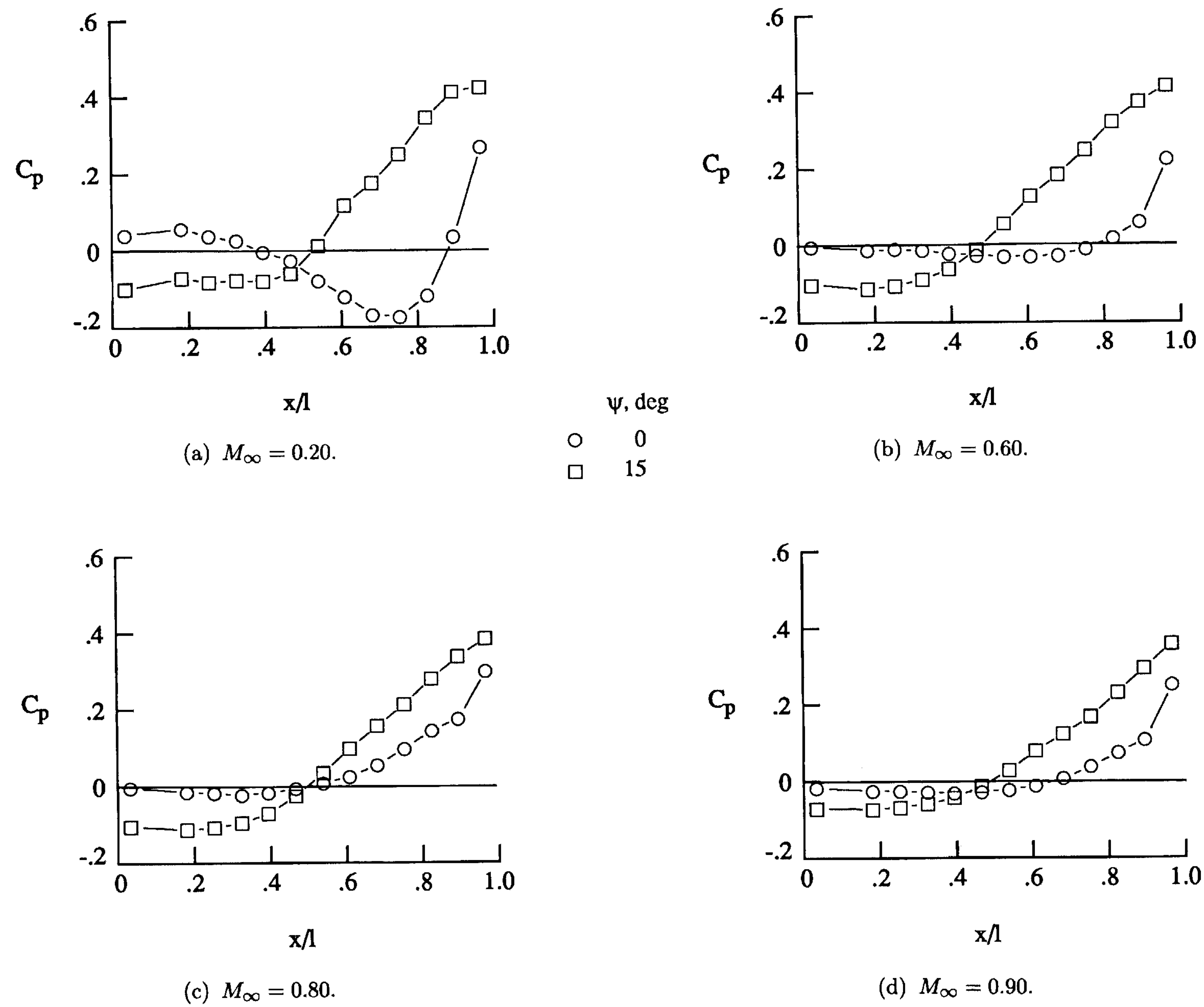

Figure 27. Effect of yaw angle on cavity pressure distributions for $l/h = 4.4$ at $R = 30 \times 10^6$ ft^{-1}.

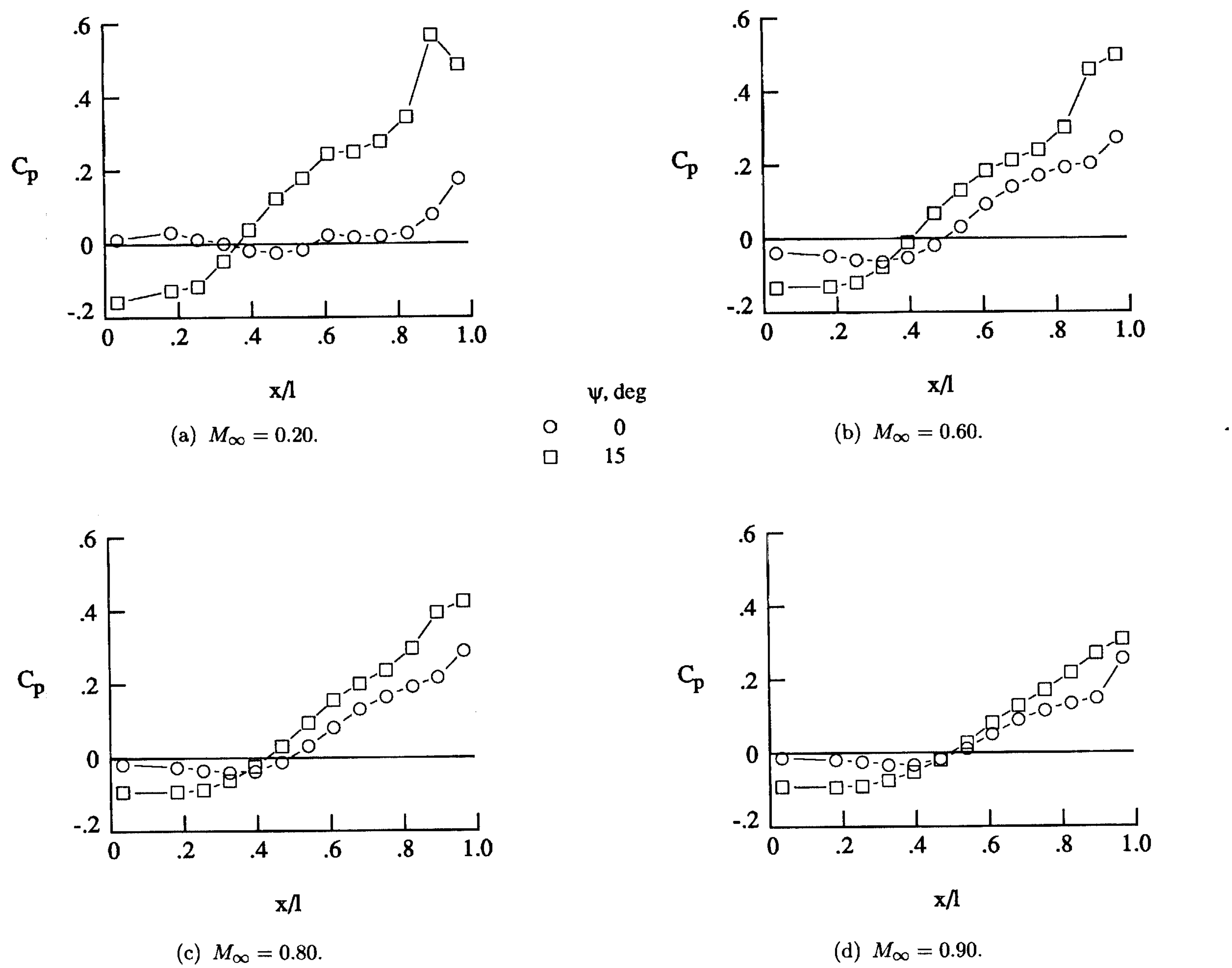

Figure 28. Effect of yaw angle on cavity pressure distributions for $l/h = 6.7$ at $R = 30 \times 10^6$ ft^{-1}.

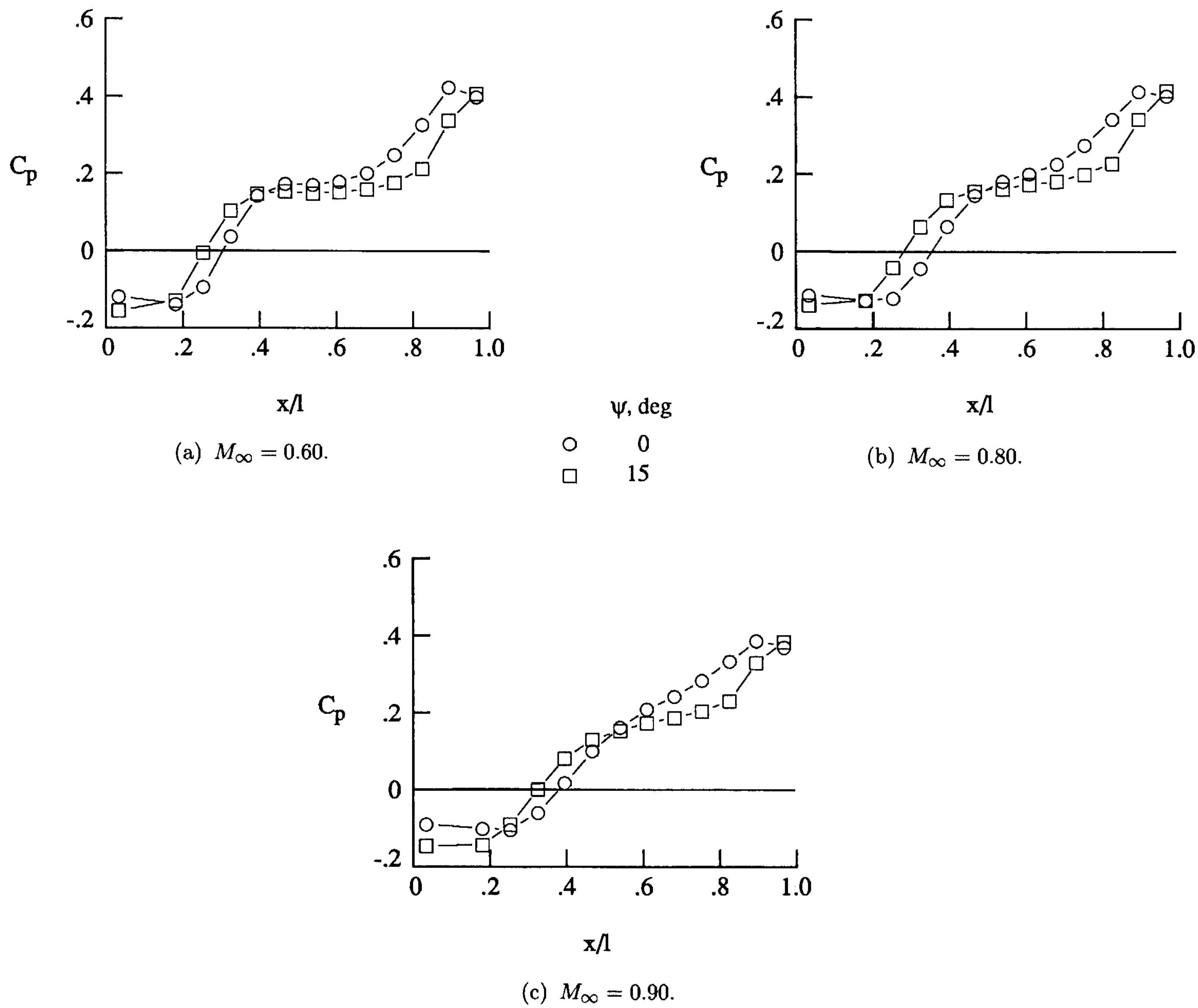

Figure 29. Effect of yaw angle on cavity pressure distributions for $l/h = 12.67$ at $R = 30 \times 10^6$ ft^{-1}.

NASA
National Aeronautics and Space Administration

Report Documentation Page

1. Report No. NASA TP-3099	2. Government Accession No.	3. Recipient's Catalog No.
4. Title and Subtitle Effects of Yaw Angle and Reynolds Number on Rectangular-Box Cavities at Subsonic and Transonic Speeds		5. Report Date July 1991
		6. Performing Organization Code
7. Author(s) E. B. Plentovich, Julio Chu, and M. B. Tracy		8. Performing Organization Report No. L-16847
9. Performing Organization Name and Address NASA Langley Research Center Hampton, VA 23665-5225		10. Work Unit No. 505-68-91-12
		11. Contract or Grant No.
12. Sponsoring Agency Name and Address National Aeronautics and Space Administration Washington, DC 20546-0001		13. Type of Report and Period Covered Technical Paper
		14. Sponsoring Agency Code

15. Supplementary Notes

16. Abstract

The effects of Reynolds number and yaw angle on pressure distributions in a rectangular-box cavity were investigated experimentally. The cavity was tested at Mach numbers from 0.20 to 0.90, Reynolds numbers from 2 to 100 $\times 10^6$ ft^{-1}, and yaw angles of 0° and 15°. Cavities were tested with length-to-depth ratios l/h of 4.4, 6.7, 12.67, and 20.0. Fluctuating- and static-pressure data on the model walls were obtained and a tabulation of the mean static-pressure data is presented. The thickness of the sidewall boundary layer entering the cavity was measured and tabulated values are provided. The Reynolds numbers tested had no significant effect on the static-pressure distributions. The effect of yaw on the cavity pressure distribution was most pronounced when the flow field was open at 0° yaw. In such cases the flow field became transitional when the cavity was positioned at 15° yaw. However, if the flow field at 0° yaw was transitional or closed, the effect of 15° yaw on the pressure distribution was very minimal. The types of flow field observed for given ranges of l/h at supersonic conditions occurred for different ranges of l/h at subsonic and transonic conditions.

17. Key Words (Suggested by Author(s)) Cavity flow Transonic speeds High Reynolds numbers Pressure measurements Turbulent boundary layer	18. Distribution Statement Unclassified—Unlimited Subject Category 02

19. Security Classif. (of this report)	20. Security Classif. (of this page)	21. No. of Pages	22. Price
Unclassified	Unclassified	52	A04

NASA FORM 1626 OCT 86 NASA-Langley, 1991

For sale by the National Technical Information Service, Springfield, Virginia 22161-2171